Delft University of Technology

Residual Stress Characterization in Microelectronic Manufacturing
An Analysis Based on Raman Spectroscopy

Yang, Zhoudong; Wang, Xinyue; Chen, Wei; Tang, Hongyu; Zhang, Rongjun; Fan, Xuejun; Zhang, Guoqi; Fan, Jiajie

DOI
10.1002/lpor.202301300

Publication date
2024

Document Version
Final published version

Published in
Laser and Photonics Reviews

Citation (APA)
Yang, Z., Wang, X., Chen, W., Tang, H., Zhang, R., Fan, X., Zhang, G., & Fan, J. (2024). Residual Stress Characterization in Microelectronic Manufacturing: An Analysis Based on Raman Spectroscopy. *Laser and Photonics Reviews*, *18*(7), Article 2301300. https://doi.org/10.1002/lpor.202301300

Important note
To cite this publication, please use the final published version (if applicable).
Please check the document version above.

Copyright
Other than for strictly personal use, it is not permitted to download, forward or distribute the text or part of it, without the consent of the author(s) and/or copyright holder(s), unless the work is under an open content license such as Creative Commons.

Takedown policy
Please contact us and provide details if you believe this document breaches copyrights.
We will remove access to the work immediately and investigate your claim.

This work is downloaded from Delft University of Technology.
For technical reasons the number of authors shown on this cover page is limited to a maximum of 10.

Green Open Access added to TU Delft Institutional Repository

'You share, we take care!' - Taverne project

https://www.openaccess.nl/en/you-share-we-take-care

Otherwise as indicated in the copyright section: the publisher is the copyright holder of this work and the author uses the Dutch legislation to make this work public.

Residual Stress Characterization in Microelectronic Manufacturing: An Analysis Based on Raman Spectroscopy

Zhoudong Yang, Xinyue Wang, Wei Chen, Hongyu Tang, Rongjun Zhang,* Xuejun Fan, Guoqi Zhang, and Jiajie Fan**

In the rapidly evolving era of information and intelligence,microelectronic devices are pivotal across various fields, such as mobile devices, big data computing, electric vehicles, and aerospace. However, the electrical performance of these devices often suffers due to residual stress from microelectronic manufacturing. This issue is compounded by the additional thermal stress that accumulates during device operation. Therefore, it is essential to understand, characterize, and control this residual stress to ensure the reliability and efficiency of microelectronic devices. Raman spectroscopy emerges as an invaluable tool for nondestructive, fast, noncontact, and precise testing of micro-scale mechanics, significantly aiding in stress and strain analysis within microelectronic manufacturing. This article aims to provide a thorough overview of the theory and application beyond a mere compilation of recent advances. Theoretically, it critically evaluates existing models that describe the Raman-stress relation. Practically, it explores the application of Raman spectroscopy in researching residual stress in various components, including substrate materials, epitaxial films, and packaging. Through a detailed examination of current applications, it highlights the significance of Raman spectroscopy in understanding micro-scale mechanics. Finally, it offers both theoretical and practical insights into the future developments of Raman-stress detection technology.

1. Introduction

In recent years, the rapid advancement of the Internet, big data, artificial intelligence, and green energy technologies has significantly elevated performance expectations for microelectronic devices, especially in demanding operating environments.[1–3] To meet these heightened demands, it is essential to leverage sophisticated microelectronic structure designs and advanced manufacturing techniques. These approaches are aimed at improving integration, reducing size, and enhancing other critical characteristics. However, a major challenge that arises in this context is the unavoidable formation of residual stresses during the manufacturing of microelectronic devices.[4] As these devices are put to use, the resulting complex stress distribution can lead to defects, cracks, delamination fractures, and other detrimental outcomes, ultimately impairing device performance.[5–7] It is evident that addressing the issue of residual stresses during the manufacturing processes is crucial for ensuring the reliability of the microelectronic devices in practical application. Furthermore, considering that microelectronic manufacturing predominantly occurs at the micro-scale, it becomes imperative to explore and understand the impacts of residual stress at this level. Employing high-resolution characterization technologies for this purpose is critically important. Research in this area has the potential to significantly reduce and refine the design and manufacturing processes, offering valuable insights for practical applications.

Z. Yang, X. Wang, W. Chen, H. Tang, R. Zhang, J. Fan
Shanghai Engineering Technology Research Center for SiC Power Device
Academy for Engineering & Technology
Fudan University
Shanghai 200433, China
E-mail: hongyu_tang@fudan.edu.cn; rjzhang@fudan.edu.cn; jiajie_fan@fudan.edu.cn

R. Zhang
School of Information Science and Technology
Fudan University
Shanghai 200433, China

X. Fan
Department of Mechanical Engineering
Lamar University
PO Box 10028, Beaumont, Texas 77710, USA

G. Zhang, J. Fan
EEMCS Faculty
Delft University of Technology
Delft 2628, The Netherlands

J. Fan
Research Institute of Fudan University in Ningbo
Ningbo 315336, China

The ORCID identification number(s) for the author(s) of this article can be found under https://doi.org/10.1002/lpor.202301300

DOI: 10.1002/lpor.202301300

© 2024 Wiley-VCH GmbH

However, the exploration of micro-scale residual stress in practical microelectronic devices is fraught with challenges that must be addressed. These challenges can be broadly categorized into 3 main aspects: First, developing new micro/nano-scale mechanical experiments and testing techniques is crucial for capturing the evolution of microstructure deformation. As electronic devices continue to become more complex and miniaturized, the existing stress testing technologies are often inadequate in terms of spatial resolution at the micro-scale level.[8,9] Furthermore, the non-destructive and accurate detection of intrinsic residual stress within electronic devices remains a significant hurdle.[10] Intrinsic stress, which results from various manufacturing processes, such as deposition, growth, modification, corrosion, aging, material interface mismatch, and inherent defects, is not adequately addressed by current testing technologies. Lastly, there is a pressing need for testing methods capable of assessing microstructural mechanics under conditions that involve multiple fields. Electronic devices often operate in environments subject to a range of interactions—such as electrical, magnetic, thermal, humidity, and chemical or electrochemical reactions.[11,12] Therefore, characterizing the mechanical properties of microstructures under such multi-field conditions has emerged as a key research focus in the field of micro-scale experimental mechanics.

To deepen our understanding of micro-scale mechanics and effectively address the associated challenges, it is imperative to develop new experiments, testing techniques, and non-destructive evaluation methods that feature enhanced spatial resolution. Raman spectroscopy emerges as a promising technique, capitalizing on the inelastic scattering mechanism between photons and molecules.[13] This technique captures characteristic information about materials at the atomic and molecular scale, enabling research on microstructure, species, and physical and chemical properties.[14,15] Given the widespread Raman activity of semiconductor materials,[16,17] Raman spectroscopy is particularly valuable for investigating the mechanical behavior and evolution process of microelectronic manufacturing at the micro-scale. It offers a powerful means to explore and comprehend the intricate mechanisms underlying microelectronic devices, boasting advantages such as high efficiency, a non-destructive and non-contact approach, and broad universality,[8,18–21] as shown in **Figure 1**. These inherent benefits enable the analysis of samples in multiple states, such as liquids and solids, without necessitating special preparation or destructive techniques. However, it is noteworthy that obtaining Raman spectra requires that the test sample exhibit Raman activity. Moreover, numerous factors must be optimized for acquiring high-quality Raman spectra in practical experiments, including mitigating fluorescence effects, ensuring sample uniformity, and fine-tuning test parameters, and equipment performance. Raman spectroscopy achieves a spatial resolution of 1 μm, making it exceptionally suited for researching mechanical behavior at the micro-scale. Through integration with near-field technology, its spatial resolution can be further enhanced to the level of hundreds of nanometers. The sensitivity of the Raman shift to stress provides a solid foundation for measuring residual stress and analyzing deformations in microelectronic devices. Its nondestructive and noncontact testing capabilities further facilitate the in situ detection of residual stress during the manufacturing process. Moreover, the use of fast line scans, surface scans, and advanced image processing technologies allows comprehensive visualization of mechanical information across the entire object.

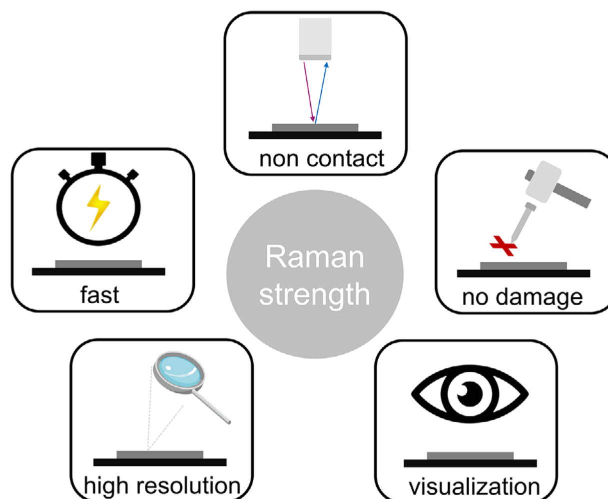

Figure 1. Overview of advantages of Raman spectroscopy technology.

This review presents a comprehensive overview of the progress in Raman spectroscopy technology for characterizing and modeling micro-scale stress in microelectronic manufacturing. We aim to provide researchers with a systematic guide to this characterization technology, expanding the practical applications of Raman spectroscopy in residual stress research within microelectronics. Complementing existing reviews on the micro-scale mechanics of microelectronics, this article highlights the distinct advantages of Raman spectroscopy in the field of stress research in microelectronics. With a focus on basic principles of Raman-stress relations, we delve into the advancements in Raman spectroscopy and its significant role in micro-scale stress research, aiming to provide a thorough understanding of the distinctive benefits it introduces to the research of micro-scale mechanics.

This review delves into the promising capabilities of Raman spectroscopy as a novel method for characterizing residual stress in microelectronic manufacturing. We provide a systematic and thorough introduction, beginning with foundational concepts and toward practical applications (**Figure 2**). Initially, we discuss the core principles of Raman spectroscopy, followed by an explanation of the basics of Raman-stress relations. This includes the characteristic equations related to lattice dynamics and elastic mechanics. In the subsequent section, we consider the strategic selection of test wavelengths under certain application conditions, focusing on 3 critical factors: detection depth, spatial resolution, and fluorescence effects. We then survey the main development trajectories of existing Raman-stress relation models. Subsequently, we delve into the main application areas of micro-scale stress research within microelectronic manufacturing, providing detailed examples to elucidate these areas. Concluding the review, we reflect on the current challenges and highlight promising directions for further developments in this field. Our goal is to shed light on the significance and potential of Raman spectroscopy in advancing the methods for characterizing residual stress in microelectronic manufacturing processes.

© 2024 Wiley-VCH GmbH

18638899, 2024, 7, Downloaded from https://onlinelibrary.wiley.com/doi/10.1002/lpor.202301300 by Tu Delft, Wiley Online Library on [15/07/2024]. See the Terms and Conditions (https://onlinelibrary.wiley.com/terms-and-conditions) on Wiley Online Library for rules of use; OA articles are governed by the applicable Creative Commons License

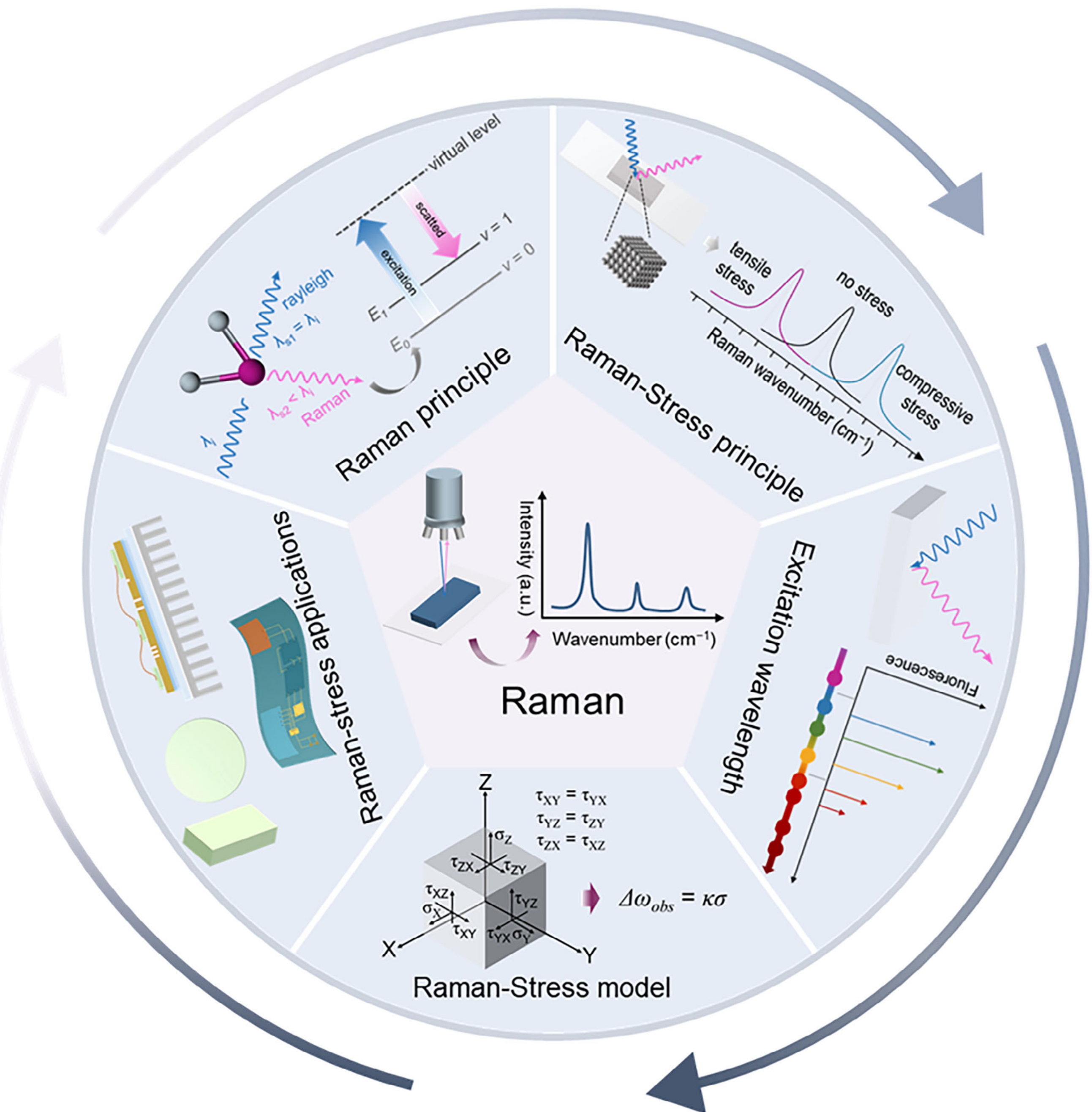

Figure 2. Schematic of the content of this review: From basic theory to practical application.

2. Basic Principles of Raman Spectroscopy

Raman measurements involve analyzing the scattered light that results from the interaction between the incoming light and the sample. This scattered light, known as Raman-scattered light, exhibits an energy different from that of the incoming light, leading to a shift in the optical frequency.[15] The frequency shift can be described as follows:

$$v_s = v_i \pm n v_j \quad (1)$$

where v_i represents the frequency of the incoming light, v_s is the frequency of the scattered light, v_j denotes the frequency of phonons in the sample, and n stands for the number of scattering series.

When n = 0, the scattering occurs without any change in energy, referred to as Rayleigh scattering. For n ≠ 0, inelastic scattering takes place, involving a change in energy; this is known as Raman scattering, as shown in **Figure 3**. The Stokes shift when the frequency of scattered light decreases, losing energy, whereas the anti-Stokes shift occurs when the frequency of scattered light

 © 2024 Wiley-VCH GmbH

18638899, 2024, 7, Downloaded from https://onlinelibrary.wiley.com/doi/10.1002/lpor.202301300 by Tu Delft, Wiley Online Library on [15/07/2024]. See the Terms and Conditions (https://onlinelibrary.wiley.com/terms-and-conditions) on Wiley Online Library for rules of use; OA articles are governed by the applicable Creative Commons License

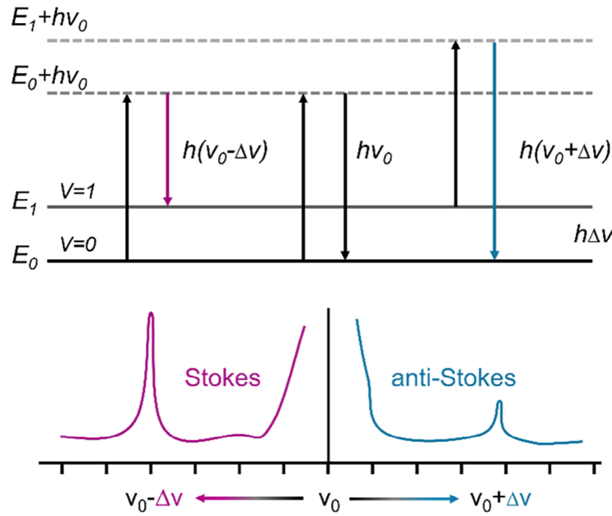

Figure 3. Schematic of Raman scattering.

increases, gaining energy. Given that energy distribution typically follows the Boltzmann distribution, the Stokes shift is more common.

Raman data are presented in a Raman spectrum, where the horizontal axis (abscissa) of the spectrogram indicates the Raman wavenumber or frequency. This unit measures the shift in wavenumber relative to the incident excitation light. Notably, the wavenumber of the Raman spectrum remains constant during the same sample test, regardless of changes in the excitation wavelength. Therefore, the abscissa of the Raman spectrum signifies the wavenumber difference (Unit: cm^{-1}) between the incoming wavelength (λ_i) and the scattered wavelength (λ_s), calculated as follows:[22]

$$\omega_0 = \omega_i - \omega_s \tag{2}$$

where ω_0 is the observed Raman frequency, ω_i is the Raman frequency of the incoming light, and ω_s is the Raman frequency of the scattered light.

The Raman spectrum originates from changes in molecular polarizability during the measurement process.[23] Given that Raman lasers emit monochromatic light, the electromagnetic theory posits that molecules experience polarization deformation under the influence of external electric fields (incoming light), producing an induced dipole moment μ. When the external electric field is small, μ is directly proportional to the electric field strength E:

$$\mu = \alpha E \tag{3}$$

Assuming the molecule vibrates in a simple harmonic manner, the change in polarizability can be expressed as a Taylor expansion around the equilibrium position:

$$\alpha = \alpha_0 + \left(\frac{\partial \alpha}{\partial \theta}\right)_0 \theta \tag{4}$$

where α_0 represents the polarizability at the equilibrium position; θ denotes the normal coordinate when the molecule vibrates.

Therefore, μ under an external electric field can be articulated as:

$$\mu = \alpha_0 E_0 \cos 2\pi v_0 t + \frac{1}{2} E_0 \theta_0 \left(\frac{\partial \alpha}{\partial \theta}\right)_0 \theta \cos 2\pi \left(v_0 - v_m\right) t + \frac{1}{2} E_0 \theta_0 \left(\frac{\partial \alpha}{\partial \theta}\right)_0 \theta \cos 2\pi \left(v_0 + v_m\right) t \tag{5}$$

where v_0 is the frequency of the incoming light, and v_m is the vibration frequency of the molecule. The first term of Equation (5) corresponds to Rayleigh scattering, the second term to Stokes scattering causing the frequency of scattered light to be smaller than that of incoming light, and the third term to blue-shifted anti-Stokes scattering.

In addition, it is observed that the probability of a molecular vibration mode's appearance in a Raman spectrum is dependent on the value of $(\partial\alpha/\partial\theta)_0$. Only when $(\partial\alpha/\partial\theta)_0 \neq 0$, which means the change of polarizability at the equilibrium position to the normal coordinate θ is nonzero. This principle is called the Raman selection rule.

The actual scattering efficiency (I) of the Raman spectrum is influenced by the polarization vectors, e_i, and e_s, which correspond to the polarization vector of the incoming and scattered light, respectively:[24]

$$I = Q \sum_k \left| e_i \cdot R_k \cdot e_s \right|^2 \tag{6}$$

where Q is a constant determined by the Raman spectrometer, and R_k represents the sample's Raman tensor, which varies according to the crystal type and vibration mode of the sample.

For further insight into the basic principles of Raman spectroscopy, we refer the readers to consult the seminal works of Manuel Cardona[25–27] and I. R. Lewis[28] for a more comprehensive understanding of Raman measurements.

3. Theoretical Basis of Raman-Stress Relation

The Raman spectrum unveils the lattice vibration characteristics of the tested sample, making Raman mechanics measurements pivotal in understanding the relationship between stress and the Raman wavenumber. This relationship, grounded in lattice dynamics theory, is elucidated by combining elastic mechanics (via the generalized Hooke's law) with material characteristic parameters. Finally, the conversion factor between material stress and Raman frequency shift can be obtained, also known as the Raman shift-stress coefficient (Unit: cm^{-1} GPa^{-1}), as shown in **Figure 4**a.

Ganesan et al. derived the expression for the lattice dynamics characteristic equation of a 3D crystal under stress, employing the harmonic oscillator model. In this framework, the potential energy function of the system is approximated using a quadratic term to account for simple harmonic vibrations:[29]

$$\begin{vmatrix} \varepsilon_{uv}K_{uv11} - \lambda & \varepsilon_{uv}K_{uv12} & \varepsilon_{uv}K_{uv31} \\ \varepsilon_{uv}K_{uv21} & \varepsilon_{uv}K_{uv22} - \lambda & \varepsilon_{uv}K_{uv32} \\ \varepsilon_{uv}K_{uv31} & \varepsilon_{uv}K_{uv32} & \varepsilon_{uv}K_{uv33} - \lambda \end{vmatrix} = 0 \tag{7}$$

where u,v = 1,2,3, and K_{uvwx} represents a component of the phonon deformation tensor, contingent on the crystal structure and optical phonon modes (w,x = 1,2,3). The strain tensors ε_{11},

© 2024 Wiley-VCH GmbH

18638899, 2024, 7, Downloaded from https://onlinelibrary.wiley.com/doi/10.1002/lpor.202301300 by Tu Delft, Wiley Online Library on [15/07/2024]. See the Terms and Conditions (https://onlinelibrary.wiley.com/terms-and-conditions) on Wiley Online Library for rules of use; OA articles are governed by the applicable Creative Commons License

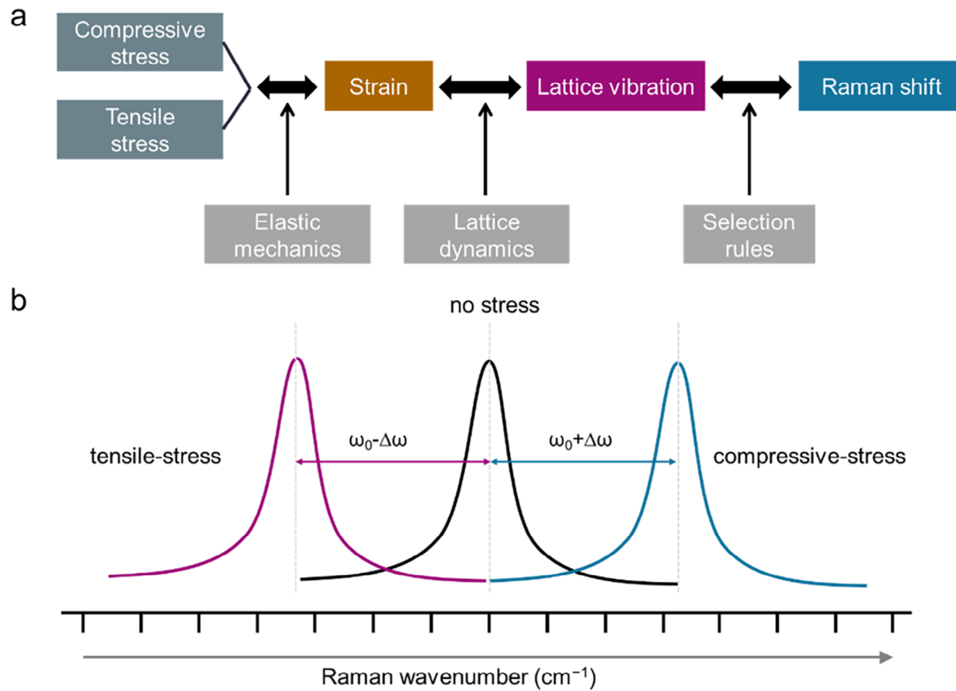

Figure 4. Raman-stress relation theory. a) Basic theoretical framework of Raman-stress relation. b) Relation between Raman shift and stress.

ε_{22} and ε_{33} correspond to strains along the X, Y, and Z directions, respectively, while ε_{12}, ε_{23}, and ε_{13} denote the strain tensors along the XY, YZ, and XZ planes, respectively. The eigenvalue of the determinant is denoted as λ_k:

$$\lambda_k = \omega_k^2 - \omega_0^2 \tag{8}$$

where ω_k signifies the Raman wavenumber under stress, and ω_0 indicates the Raman wavenumber without stress.

The characteristic equation of lattice dynamics elucidated above provides insights into the stress response to internal spacing within the sample. Raman spectroscopy thus aims to detect changes in atomic spacing (strain) within the material lattice under stress. This technique seeks to establish a functional relationship between changes in the Raman wavenumber and applied stress in the Raman spectra. By defining the change in the Raman wavenumber as the difference between the wavenumber under stress and the intrinsic wavenumber without stress, we observe macroscopic phenomena in the Raman spectrum attributable to stress. Specifically, the Raman wavenumber shifts toward red (decreases) under tensile-stress. Conversely, under compressive-stress, the Raman wavenumber undergoes a blueshift (increases),[30–32] as shown in Figure 4b. Given that the Raman wavenumber change caused by stress is typically small compared to the peak position value (ω_0) without stress, this change can be further approximated and simplified to understand the wavenumber change before and after stress application:[29]

$$\Delta\omega_k = \omega_k - \omega_0 \approx \frac{\omega_k^2 - \omega_0^2}{2\omega_0} = \frac{\lambda_k}{2\omega_0} \tag{9}$$

In Raman spectroscopy, each characteristic peak signifies the interaction between incoming light and specific atomic vibrational modes. It has been observed in the literature that[33–35] the peak shift value under stress, as derived from lattice dynamics equations, can present multiple solutions, resulting in a degenerate state. Specifically, the number of solutions corresponds to the number of Raman tensors associated with the chosen vibrational modes. Consequently, when the Raman tensor count for a selected vibration mode is more than one, the observed shift in Raman peaks reflects the combination of multiple degenerate states.

Due to the small deformation of the material, there exists a linear relationship between stress and strain, facilitating the application of the generalized Hooke's law in elastic mechanics:

$$\sigma = C\varepsilon \tag{10}$$

where C denotes the elastic coefficient tensor specific to the material, while σ and ε represent the stress and strain tensors, respectively.

Following the derivation of the Raman shift from the lattice dynamics equation, when the count of Raman tensors associated with the chosen vibrational modes exceeds one, the Raman characteristic peak in the measured spectrum is formed by the superposition of multiple degeneracy states. Consequently, even under conditions of micro-deformation, while the Raman wavenumber shifts, the degeneracy state persists without significant peak splitting. Therefore, the observed changes in the Raman wavenumber under these conditions also arise from the superposition of multiple degenerate states. To calculate this shift, the following equation must be emphasized:[29,36]

$$\Delta\omega_{obs} = \frac{\sum_{k=1}^{3} \Delta\omega_k I_k}{\sum_{k=1}^{3} I_k} \tag{11}$$

© 2024 Wiley-VCH GmbH

18638899, 2024, 7, Downloaded from https://onlinelibrary.wiley.com/doi/10.1002/lpor.202301300 by Tu Delft, Wiley Online Library on [15/07/2024]. See the Terms and Conditions (https://onlinelibrary.wiley.com/terms-and-conditions) on Wiley Online Library for rules of use; OA articles are governed by the applicable Creative Commons License

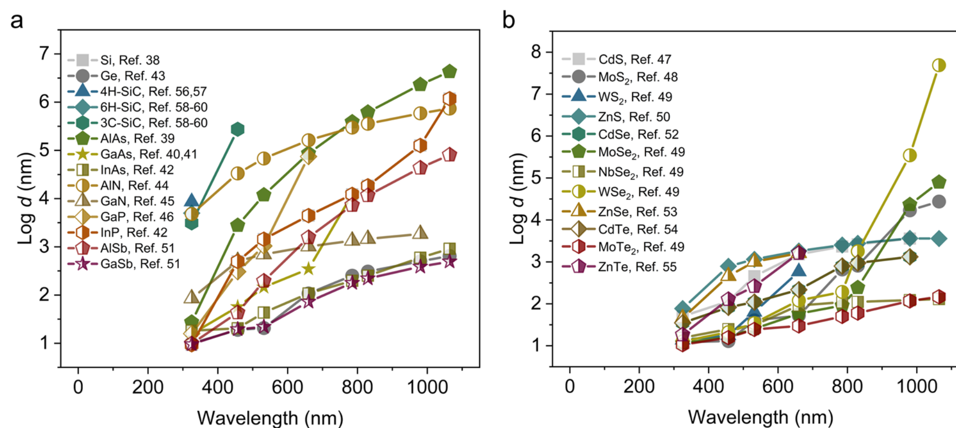

Figure 5. Maximum penetration depth of laser light with different wavelengths in semiconductor materials. a) Log *d*-laser wavelength relationship diagram of Si, Ge, SiC, and N compound semiconductor. b) Log *d*-laser wavelength relationship diagram of chalcogenide semiconductor.

Equation (11) indicates that the degenerate states are amalgamated and linearly superimposed. When integrated with Equations (3–7), a final linear relationship is established, correlating the change in Raman displacement to the stress applied before and after, as outlined below:

$$\Delta\omega_{obs} = \kappa\sigma \tag{12}$$

where the slope κ provides the Raman shift-stress coefficient.

4. Raman Excitation Light Selection Basis

In microelectronic micro-scale stress research, Raman spectroscopy is a non-destructive and contact-free detection method. A key test parameter is the maximum penetration depth (d), which determines the specific range of the actual stress test. The laser used determines the Raman spectrometer's excitation wavelength, resulting in various penetration depths for different material samples. Hence, selecting an appropriate laser wavelength is important for obtaining accurate experimental results in micro-scale stress research. The formula for calculating the maximum penetration depth for different wavelengths is:[37]

$$d = \frac{2.3}{2\alpha} \tag{13}$$

where α (Unit: cm^{-1}) represents the light absorption coefficient of the test material at the incoming wavelength (λ_i).

Figure 5 illustrates the maximum penetration depths for main semiconductor materials at various excitation wavelengths. Data analysis from the figure indicates a consistent trend: the maximum detection depth increases with the wavelength for most semiconductor materials. This trend is instrumental in selecting an appropriate excitation wavelength to meet the depth requirements of Raman measurements for different materials. The data corresponding to the specific excitation wavelength and maximum penetration depths are detailed in **Table 1**. The actual detection depth is also influenced by factors such as the sample's surface morphology, the laser power employed, the choice of scattering angle, and the focus depth during experimentation.

Moreover, the excitation wavelength directly influences the Raman spatial resolution (D), which is influenced by the laser spot size. The diameter of the laser spot can be calculated under the diffraction-limited condition:[61]

$$D = \frac{0.61\lambda_i}{NA} \tag{14}$$

where λ_i is the wavelength of the incident laser and NA is the numerical aperture of the microscope objective used. According to Equation (14), the laser spot size is a function of λ_i and the NA of the microscope objective lens. To maintain an appropriate D value with long-wavelength excitation light, it becomes imperative to appropriately increase the NA of the microscope objective.

The choice of excitation wavelength also needs to consider the laser's interaction with the sample. If the excitation light satisfies the conditions for the sample to absorb photons of characteristic frequency, electrons move from the ground-state to the first electronic excited state or higher. These electrons then relax to the lowest energy level of the first excited state before moving to various vibrational energy levels of the ground-state, emitting fluorescence. This fluorescence can interfere with identifying characteristic Raman peak positions and their full width at half maximum (FWHM).[62,63] However, using lasers in the ultraviolet and infrared bands can significantly mitigate this fluorescence effect on data analysis, as shown in **Figure 6a**. With ultraviolet light excitation, although fluorescence occurs, the Raman and fluorescence signals do not overlap[64] (Figure 6b). Conversely, infrared light excitation less readily excites ground-state electrons, reducing fluorescence effects. Furthermore, Figure 6c provides a concise overview of the strengths and weaknesses of the 3 excitation bands: ultraviolet, visible, and infrared.

In conclusion, the data provide valuable insights for selecting suitable excitation wavelengths for Raman measurements in Table 1, considering detection depth and spatial resolution. Moreover, understanding the impact of excitation wavelength on fluorescence background helps in making informed decisions for accurate Raman measurements.

© 2024 Wiley-VCH GmbH

18638899, 2024, 7, Downloaded from https://onlinelibrary.wiley.com/doi/10.1002/lpor.202301300 by Tu Delft, Wiley Online Library on [15/07/2024]. See the Terms and Conditions (https://onlinelibrary.wiley.com/terms-and-conditions) on Wiley Online Library for rules of use; OA articles are governed by the applicable Creative Commons License

Table 1. Detection depth in semiconductor materials under different wavelengths.

		325 nm	457 nm	532 nm	660 nm	785 nm	830 nm	980 nm	1064 nm
Si [38]	α cm^{-1}	1.23×10^{6}	2.31×10^{4}	7.99×10^{3}	2.59×10^{3}	9.46×10^{2}	6.24×10^{2}	91.5	9.76
	d nm	9.33	4.98×10^{2}	1.44×10^{3}	4.44×10^{3}	1.22×10^{4}	1.84×10^{4}	1.26×10^{5}	1.18×10^{6}
AlAs [39]	α cm^{-1}	4.2×10^{5}	4.14×10^{3}	9.68×10^{2}	1.33×10^{2}	29.5	18.5	4.97	2.69
	d nm	27.4	2.78×10^{3}	1.19×10^{4}	8.65×10^{4}	3.90×10^{5}	6.20×10^{5}	2.31×10^{6}	4.28×10^{6}
GaAs [40,41]	α cm^{-1}	7.38×10^{5}	2.02×10^{5}	7.94×10^{4}	3.30×10^{4}	1.42×10^{4}	8.66×10^{3}	0	0
	d nm	15.6	56.9	1.45×10^{2}	3.49×10^{2}	1.22×10^{4}	1.84×10^{4}	/	/
InAs [42]	α cm^{-1}	6.33×10^{5}	5.64×10^{5}	2.66×10^{5}	1.06×10^{5}	5.79×10^{4}	4.56×10^{4}	1.93×10^{4}	1.26×10^{4}
	d nm	18.2	20.4	43.3	1.08×10^{2}	1.98×10^{2}	2.52×10^{2}	5.95×10^{2}	9.13×10^{2}
Ge [43]	α cm^{-1}	1.16×10^{6}	$6.04{\times}10^{5}$	5.55×10^{5}	1.06×10^{5}	4.57×10^{4}	3.76×10^{4}	2.29×10^{4}	1.79×10^{4}
	d nm	9.94	19.0	20.7	1.08×10^{2}	2.52×10^{2}	3.06×10^{2}	5.03×10^{2}	6.44×10^{2}
AlN [44]	α cm^{-1}	2.40×10^{4}	3.45×10^{2}	1.70×10^{2}	70.9	38.6	32.2	19.6	15.6
	d nm	4.79×10^{3}	3.33×10^{4}	6.78×10^{4}	1.62×10^{5}	2.98×10^{5}	3.57×10^{5}	5.88×10^{5}	7.38×10^{5}
GaN [45]	α cm^{-1}	1.35×10^{5}	2.27×10^{4}	1.65×10^{4}	1.13×10^{4}	8.57×10^{3}	7.88×10^{3}	6.20×10^{3}	1.21×10^{4}
	d nm	85.2	5.07×10^{2}	6.96×10^{2}	1.02×10^{3}	1.34×10^{3}	1.46×10^{3}	1.85×10^{3}	/
GaP [46]	α cm^{-1}	7.29×10^{5}	3.77×10^{4}	1.10×10^{4}	1.54×10^{2}	0	0	0	0
	d nm	15.8	3.05×10^{2}	1.04×10^{3}	7.46×10^{4}	/	/	/	/
InP [42]	α cm^{-1}	6.92×10^{5}	1.96×10^{5}	9.53×10^{4}	5.83×10^{4}	4.23×10^{4}	3.26×10^{4}	8.47×10^{2}	7.14×10^{2}
	d nm	9.33	4.98×10^{2}	1.44×10^{3}	4.44×10^{3}	1.22×10^{4}	1.84×10^{4}	1.26×10^{5}	1.18×10^{6}
CdS [47]	α cm^{-1}	2.27×10^{5}	1.01×10^{5}	2.53×10^{4}	7.56×10^{3}	4.95×10^{3}	4.40×10^{3}	3.18×10^{3}	/
	d nm	50.7	1.14×10^{2}	4.54×10^{2}	1.52×10^{3}	2.33×10^{3}	2.62×10^{3}	3.60×10^{3}	/
MoS_2 [48]	α cm^{-1}	9.39×10^{5}	8.94×10^{5}	2.84×10^{5}	$2.21{\times}10^{5}$	1.75×10^{4}	1.42×10^{4}	6.79×10^{3}	4.18×10^{3}
	d nm	12.2	12.9	40.5	52.1	6.59×10^{2}	8.10×10^{2}	1.69×10^{4}	2.75×10^{4}
WS_2 [49]	α cm^{-1}	8.36×10^{5}	6.50×10^{5}	1.80×10^{5}	1.96×10^{4}	0	0	0	0
	d nm	13.8	17.7	64.0	5.88×10^{2}	/	/	/	/
ZnS [50]	α cm^{-1}	1.49×10^{5}	1.46×10^{4}	1.00×10^{4}	6.30×10^{3}	4.57×10^{3}	4.15×10^{3}	3.16×10^{3}	/
	d nm	77.1	7.86×10^{2}	1.15×10^{3}	1.82×10^{3}	2.52×10^{3}	2.77×10^{3}	3.64×10^{3}	3.60×10^{3}
AlSb [51]	α cm^{-1}	1.17×10^{6}	2.66×10^{5}	5.90×10^{4}	7.36×10^{3}	1.58×10^{3}	9.89×10^{2}	2.65×10^{2}	1.44×10^{2}
	d nm	9.80	43.2	1.95×10^{2}	1.56×10^{3}	7.29×10^{3}	1.16×10^{4}	4.33×10^{4}	8.09×10^{4}
GaSb [51]	α cm^{-1}	1.21×10^{6}	$5.90{\times}10^{5}$	4.29×10^{5}	1.58×10^{5}	6.46×10^{4}	5.20×10^{4}	2.97×10^{4}	2.32×10^{4}
	d nm	9.54	19.5	21.9	72.6	1.78×10^{2}	2.21×10^{2}	3.87×10^{2}	4.96×10^{2}
CdSe [52]	α cm^{-1}	3.27×10^{5}	$1.39{\times}10^{5}$	1.05×10^{5}	5.59×10^{4}	1.45×10^{4}	1.22×10^{4}	8.70×10^{3}	/
	d nm	35.2	82.6	1.10×10^{2}	2.17×10^{2}	7.94×10^{2}	9.40×10^{2}	1.32×10^{3}	/
$MoSe_2$ [49]	α cm^{-1}	9.92×10^{5}	7.02×10^{5}	4.52×10^{5}	1.97×10^{5}	1.26×10^{5}	4.74×10^{4}	4.97×10^{2}	1.45×10^{2}
	d nm	11.6	16.4	25.4	58.3	91.0	2.43×10^{2}	2.31×10^{4}	7.91×10^{4}
$NbSe_2$ [49]	α cm^{-1}	7.44×10^{5}	4.62×10^{5}	3.69×10^{5}	1.26×10^{5}	1.05×10^{5}	1.04×10^{5}	9.34×10^{4}	8.81×10^{4}
	d nm	15.5	24.9	31.1	91.6	1.09×10^{2}	1.11×10^{2}	1.23×10^{2}	1.30×10^{2}
WSe_2 [49]	α cm^{-1}	9.01×10^{5}	5.44×10^{5}	3.31×10^{5}	9.60×10^{4}	6.00×10^{4}	6.42×10^{3}	33.1	2.35×10^{-2}
	d nm	12.7	21.1	34.7	$1.20{\times}10^{2}$	1.92×10^{2}	1.79×10^{3}	3.48×10^{5}	4.89×10^{7}
ZnSe [53]	α cm^{-1}	2.52×10^{5}	2.51×10^{4}	1.13×10^{4}	7.16×10^{3}	/	/	/	/
	d nm	45.6	4.58×10^{2}	1.01×10^{3}	1.61×10^{3}	/	/	/	/
CdTe [54]	α cm^{-1}	6.33×10^{5}	1.30×10^{5}	8.76×10^{4}	6.00×10^{4}	2.18×10^{4}	7.57×10^{3}	4.83×10^{3}	/
	d nm	35.2	82.6	1.10×10^{2}	$2.17{\times}10^{2}$	$7.94{\times}10^{2}$	$9.40{\times}10^{2}$	1.32×10^{3}	/
$MoTe_2$ [49]	α cm^{-1}	1.08×10^{6}	$7.31{\times}10^{5}$	4.69×10^{5}	3.87×10^{5}	2.30×10^{5}	1.91×10^{5}	9.87×10^{4}	7.82×10^{4}
	d nm	10.6	15.7	24.5	29.7	50.1	60.2	1.17×10^{2}	1.47×10^{2}
ZnTe [55]	α cm^{-1}	6.29×10^{5}	9.01×10^{4}	4.40×10^{4}	7.16×10^{3}	/	/	/	/
	d nm	18.3	1.28×10^{2}	2.62×10^{2}	1.61×10^{3}	/	/	/	/
4H-SiC [56,57]	α cm^{-1}	1.33×10^{3}	0	0	0	0	0	0	0
	d nm	8.65×10^{3}	/	/	/	/	/	/	/
6H-SiC [58–60]	α cm^{-1}	2.30×10^{3}	0	0	0	0	0	0	0
	d nm	5.00×10^{3}	/	/	/	/	/	/	/
3C-SiC [58–60]	α cm^{-1}	3.66×10^{3}	42.0	0	0	0	0	0	0
	d nm	3.14×10^{3}	$2.74{\times}10^{5}$	/	/	/	/	/	/

© 2024 Wiley-VCH GmbH

18638899, 2024, 7, Downloaded from https://onlinelibrary.wiley.com/doi/10.1002/lpor.202301300 by Tu Delft, Wiley Online Library on [15/07/2024]. See the Terms and Conditions (https://onlinelibrary.wiley.com/terms-and-conditions) on Wiley Online Library for rules of use; OA articles are governed by the applicable Creative Commons License

18638899, 2024, 7, Downloaded from https://onlinelibrary.wiley.com/doi/10.1002/lpor.202301300 by Tu Delft, Wiley Online Library on [15/07/2024]. See the Terms and Conditions (https://onlinelibrary.wiley.com/terms-and-conditions) on Wiley Online Library for rules of use; OA articles are governed by the applicable Creative Commons License

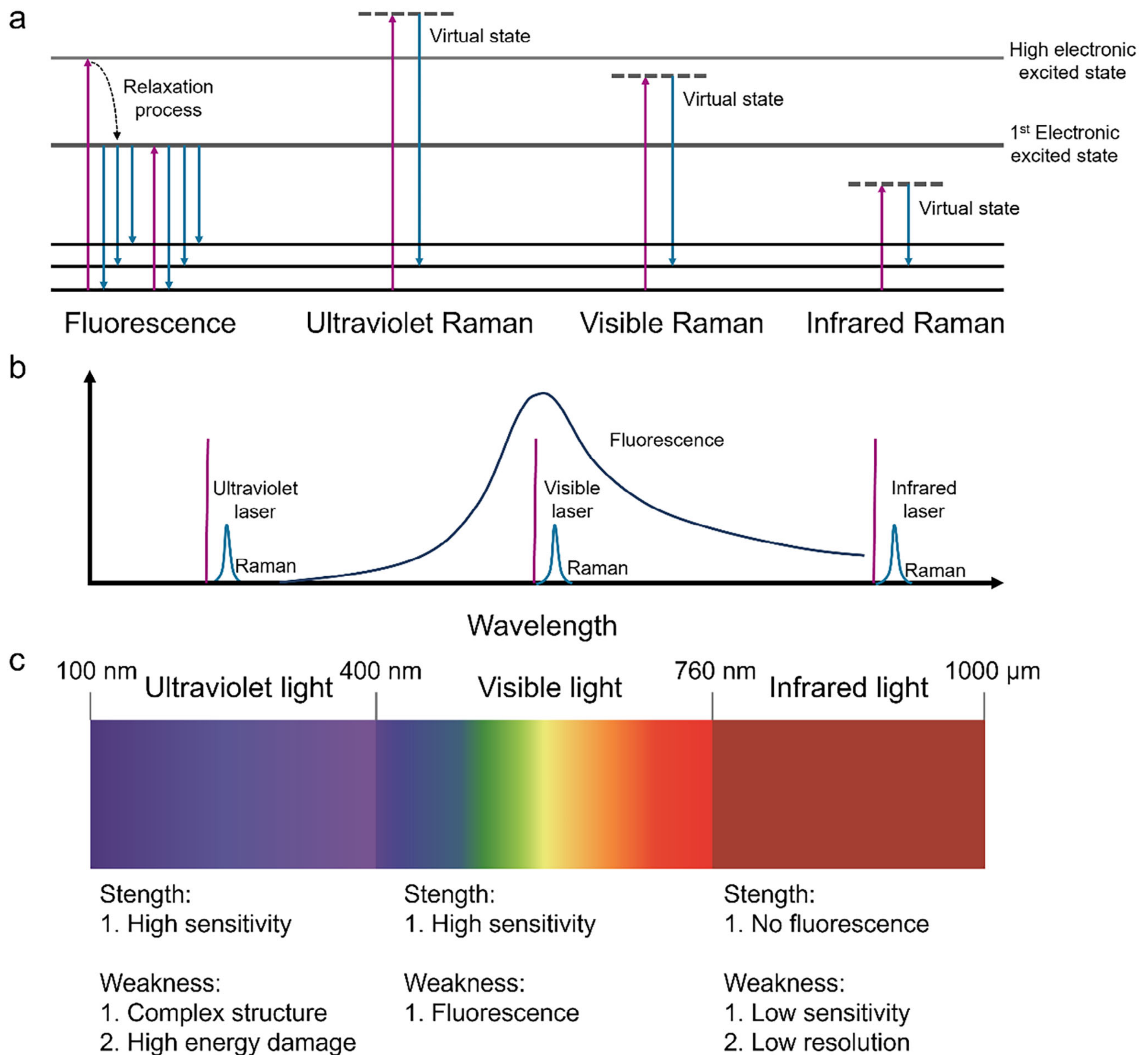

Figure 6. Reasonable selection of light band. a) Fluorescence effect and Raman scattering under different light bands. b) Influence of fluorescence effect on spectra under different light bands. c) Strength and weakness of each excitation light band.

5. Development Process of Raman-Stress Relation Model

The core of researching micro-scale mechanics in microelectronics using Raman spectroscopy centers on developing stress prediction models tailored to specific research subjects. The accuracy of the model directly influences the precision of stress numerical calculations. Thus, a high-precision model holds significant reference value and practical applications for stress research, mechanical reliability analysis, and guidance in manufacturing processes. This section delves into the Raman-stress relation models cited in various research, summarizing its key developmental process, as shown in **Figure 7** insights for refining existing models and proposing new high-precision stress models.

Historically, the exploration of Raman-stress relation models has advanced significantly. Initially, the research work on Raman-stress relation models can be traced back to the research on silicon (Si) Raman spectroscopy under static uniaxial stress conducted in 1970.[65] Researchers noted the shift and splitting of Raman peaks of optical phonons due to applied uniaxial stress, leading to the identification of a phenomenological coefficient that describes the "spring constant" of phonons that changes with strain. This marked the beginning of mechanical stress in microelectronic devices based on Raman technology has gradually attracted attention and development. Raman spectroscopy has been applied to investigate stress-related phenomena in various microelectronic components, such as the local stress in "bird's beak" structures during Si local oxidation,[66] residual

 © 2024 Wiley-VCH GmbH

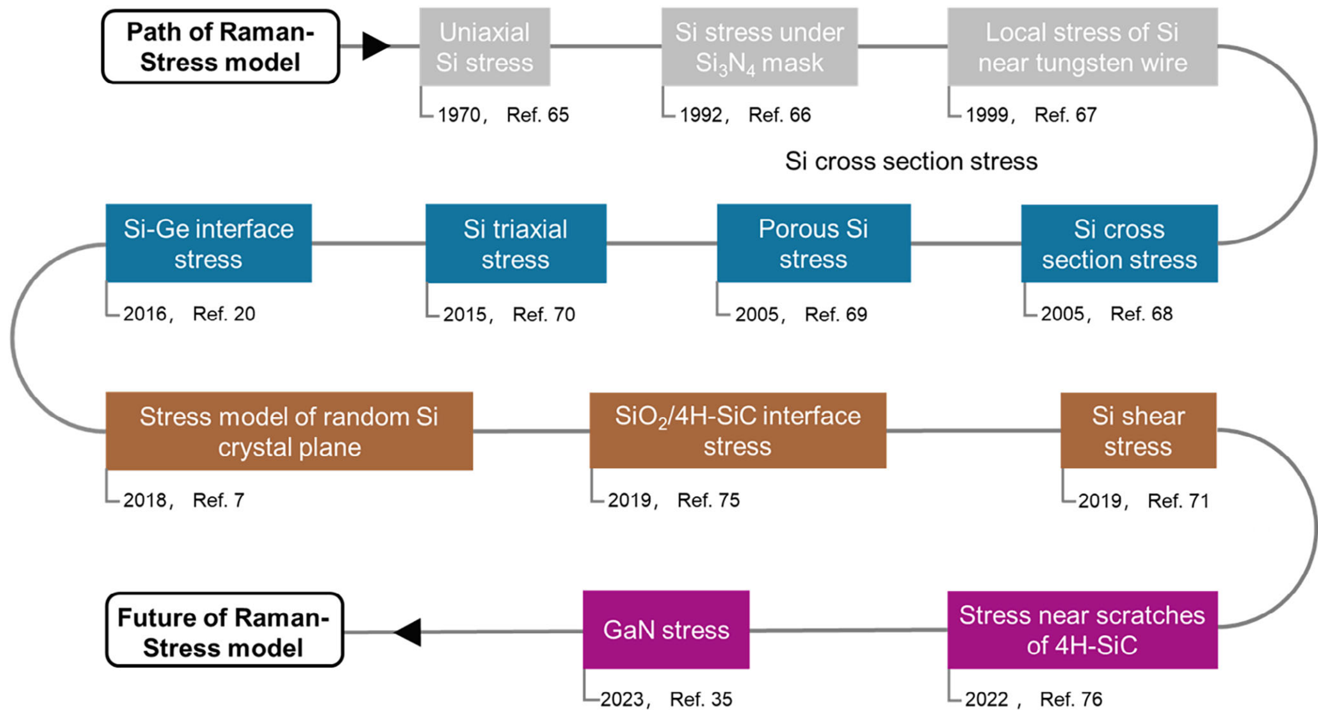

Figure 7. Roadmap of Raman-stress relation models with major achievements.

stress in Si substrates,[67,68] stress across silicon-based heterojunction interfaces,[20] and interface stress in microelectromechanical systems (MEMS).[69]

In silicon-based Raman-stress relation research, 3 major advancements are noteworthy: a) the development of a Raman-stress relation model accounting for actual triaxial stress conditions,[70] optimizing the simpler plane stress prediction models based on uniaxial or biaxial stresses assumptions; b) the introduction of a prediction equation for assessing stress on different crystalline Si planes.[7] This advancement establishes a comprehensive framework for stress analysis of different crystal planes in Si, greatly enhancing the understanding of stress distribution in silicon-based devices and its impact on different device structures. c) In actual situations, when an object deforms due to external factors (load, temperature changes, etc.), internal stress will be formed in any section inside it. Internal stress can be decomposed into normal stress perpendicular to the cross-section and shear stress tangent to the cross-section. Therefore, a sole consideration of the three-axis normal stress proves inadequate for precise force analysis of the object. To address this limitation, researchers further incorporated actual shear stress conditions to develop a new type of Si crystal Raman-stress relation model.[71] This significant improvement greatly reduces calculation errors caused by previously neglecting the effects of shear stress. These developments have propelled forward the understanding of stress in silicon-based materials, offering significant promise for optimizing the design, performance, and reliability of microelectronic devices.

Moreover, the immense potential of third-generation semiconductors[72,73] has expanded the application of Raman spectroscopy to stress characterization in novel semiconductor materials such as silicon carbide (SiC)[74–77] and gallium nitride (GaN). [35,78,79] Researchers have developed Raman-stress relation models for these materials, facilitating accurate stress characterization and broadening their applications.

In summary, while the development of Raman-stress relation models has predominantly focused on silicon—attributed to its longstanding predominance in semiconductor device markets and manufacturing, recent advancements in third-generation semiconductors, such as SiC and GaN, have catalyzed a growing interest in investigating stress/strain in these emerging materials.

6. Application of Raman Characterization and Modeling in Microelectronic Manufacturing

By combining theoretical Raman-stress relation models with experimental Raman measurement techniques, we can efficiently calculate and visualize the distribution of residual stress within a research object. This process of residual stress testing is simple, swift, and non-destructive, making it highly suitable for actual production and manufacturing processes. In this section, we categorize and discuss the main applications of this technology in the key processes of microelectronics manufacturing (**Figure 8**). This discussion aims to deepen the understanding of this technology and inspire new insights and approaches for its application across various research fields.

6.1. Substrate Materials

Substrate materials are crucial in the production of semiconductor devices. The stress within these materials significantly impacts both the manufacturing process and the performance of

© 2024 Wiley-VCH GmbH

18638899, 2024, 7, Downloaded from https://onlinelibrary.wiley.com/doi/10.1002/lpor.202301300 by Tu Delft, Wiley Online Library on [15/07/2024]. See the Terms and Conditions (https://onlinelibrary.wiley.com/terms-and-conditions) on Wiley Online Library for rules of use; OA articles are governed by the applicable Creative Commons License

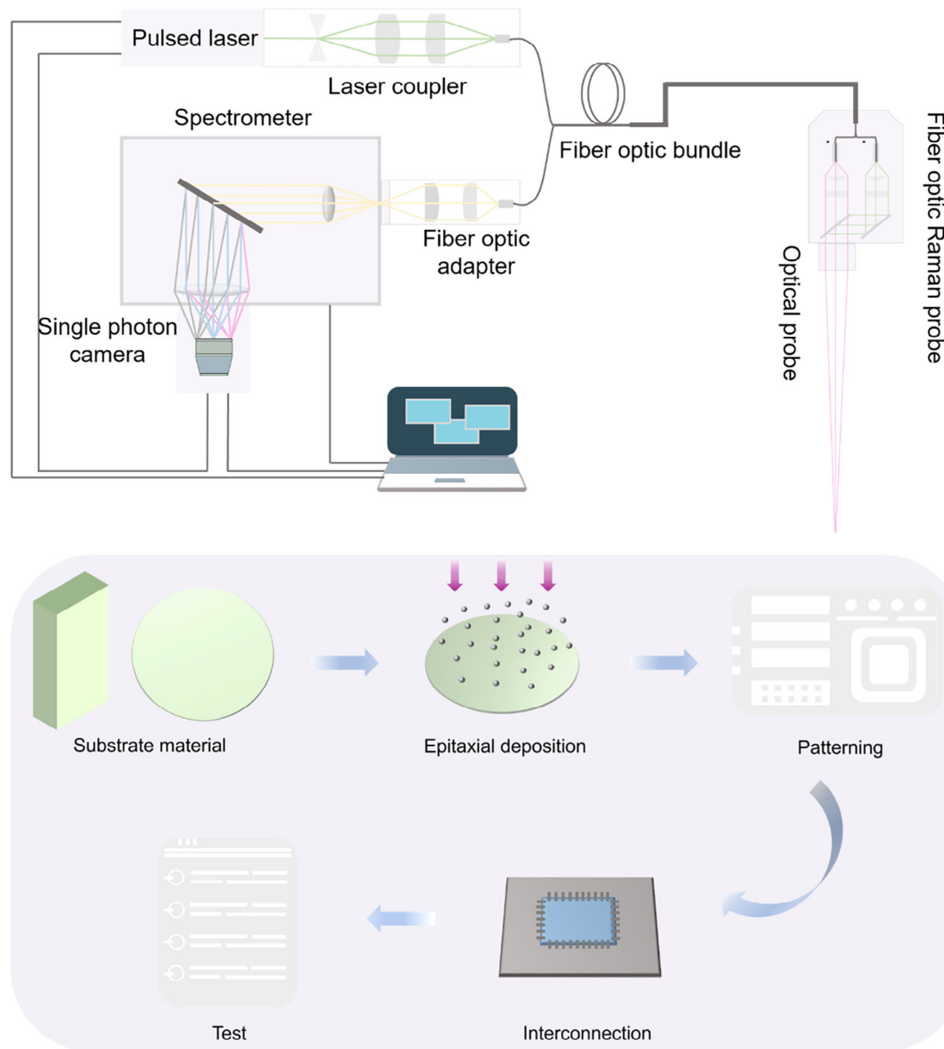

Figure 8. Schematic of application of Raman in the detection of residual stress in the field of microelectronics manufacturing.

the final product. Therefore, accurately detecting and evaluating this stress is crucial. This assessment helps identify areas of high-stress concentration, offering essential guidance for implementing strategies to alleviate and mitigate stress in industrial settings. A comprehensive analysis of stress levels in substrate materials allows manufacturers to optimize the performance and reliability of their devices. Stress detection is crucial for enhancing the yield and quality of semiconductor products, making it a vital component of semiconductor manufacturing.

6.1.1. Silicon (Si)

The significance of silicon-based semiconductors in practical applications and research is well recognized, leading to a focused effort on stress analysis in Si substrates. The exploration of Raman-stress relationships within single-crystal Si dates back to 1970 when Anastassakis et al.[65] conducted pioneering research on the impacts of static uniaxial stress on the optical phonon frequencies of single-crystal Si. However, due to the limitations of Raman spectroscopy at that time, this method of stress detection was not widely adopted for many years. Nevertheless, advancements in Raman technology from the late 20th century onward have facilitated significant progress in the research of Si stress distribution. Key achievements in this period encompass the measurement of Si Raman-stress relation,[80,81] stress analysis in Si defect regions,[82–84] exploration of residual stress in Si machining processes,[85] and comprehensive characterization of Si wafer stress,[86] among others. However, these studies have predominantly focused on the conventional (001) crystal plane of Si, constraining their broader applicability due to the anisotropic nature of different crystal planes.

To address the previously mentioned limitations, Huang et al.[87] conducted experiments to establish the Raman-stress relation for the Si (111) crystal plane. By conducting multiple measurements with varying directions of scattered light and employing the least-squares method for linearly fitting the data, they derived conclusive results, as shown in **Figure 9**. This precise determination of the Raman-stress relation within single-crystal Si facilitated subsequent investigations by Pogue

 © 2024 Wiley-VCH GmbH

18638899, 2024, 7, Downloaded from https://onlinelibrary.wiley.com/doi/10.1002/lpor.202301300 by Tu Delft, Wiley Online Library on [15/07/2024]. See the Terms and Conditions (https://onlinelibrary.wiley.com/terms-and-conditions) on Wiley Online Library for rules of use; OA articles are governed by the applicable Creative Commons License

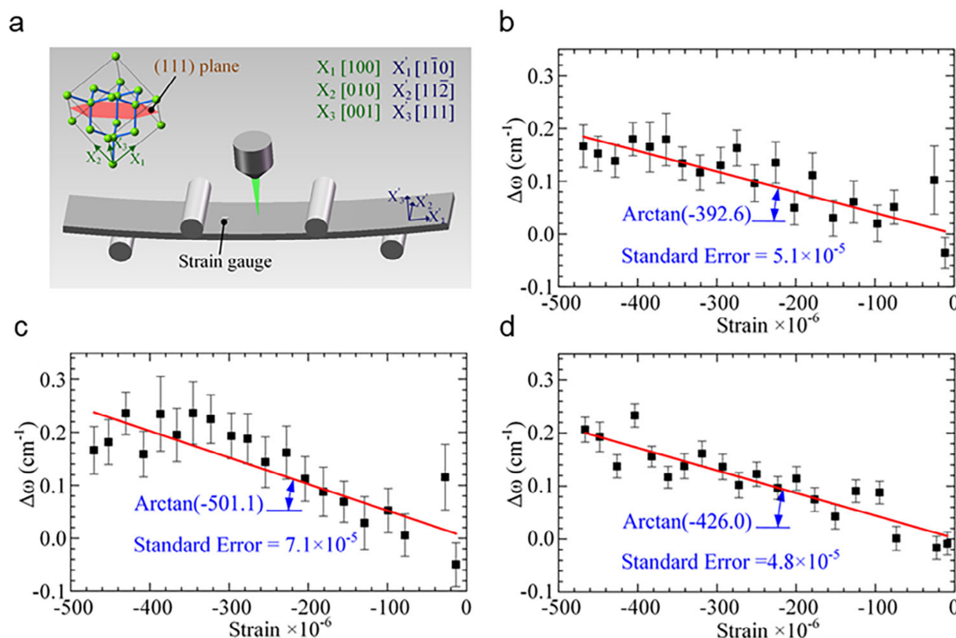

Figure 9. Raman-stress relation of Si. a) Schematic of sample test experiment. Calibration results of Raman shift-stress relationship when incoming light is in X'_1 direction and scattered light is in b) X'_1, c) X'_2, and d) $X'_1 + X'_2$. Reproduced under the terms of the CC-BY 4.0 license.[87] Copyright 2017, The Authors, published by AIP Publishing.

et al.,[88] who expanded this relationship to examine the residual stress induced by thermal gradients and wire sawing processes in photovoltaic polycrystalline Si wafers during casting. The research involved stepwise etching of multi-crystalline Si diamond wire sawing (DWS) and loose abrasive wire sawing (LAWS) wafers at different depths, followed by characterization of residual stress in specific regions on each wafer using polarized confocal Raman microscopy. The results indicated that both DWS and LAWS processes induced compressive-stress on the multi-crystal Si wafer's surface layer, with LAWS resulting in less surface residual stress compared to DWS. Additionally, while residual stress in DWS wafers transitioned from compression to tension with increasing etch depth, LAWS wafers exhibited a consistently compressive trend.

Given that current silicon-based Raman-stress relations ignore shear stress, a notable gap exists between actual and measured results. Therefore, it is imperative to investigate the real impact of neglecting the shear stress component in Raman-stress measurements of crystalline Si. Addressing this, Qiu et al.[89] conducted experiments with (001) and (111) Si wafer samples, each shaped into 4 mm regular octagons and subjected to a uniaxial compressive force along the X-axis at a 45° angle from the X-axis (**Figure** 10a,b). Utilizing a micro-Raman laser instrument, they performed point-by-point surface scans along the X-axis and calculated the average Raman shift, comparing experimental values to theoretical predictions for each crystal plane based on the triaxial stress model, as shown in Figure 10c. Their results indicated that shear stress did not affect the Raman shift on the (001) plane, but significantly impacted the (111) plane, resulting in an error of ≈3.16%. This led to the quantitative determination of each stress tensor in crystalline Si through polarized Raman spectroscopy, dubbed as a "strain rosette", which incorporates the shear stress component,[71] shown in Figure 10d. By adjusting the angles between the width direction of samples S_1 and S_2, and the X-axis to 0° and 45°, respectively, they achieved varying stress states in the sample coordinate system under uniaxial compressive-stress (Figure 10e). The polarized Raman spectroscopy test results closely matched the model predictions, demonstrating the significant influence of shear stress on the Raman shift-stress coefficient, which varied with the polarization angle of the incoming light, as evidenced in Figure 10f.

6.1.2. Silicon Carbide (SiC)

As a prominent example of third-generation wide-bandgap semiconductors, SiC has garnered substantial interest from both industry and academia due to its remarkable electrical properties compared to conventional silicon-based semiconductors.[90] The detection of residual stress in SiC is significantly important. Leveraging the silicon-based Raman-stress detection method, efforts have been made to adapt this technology for stress analysis in SiC crystals. For instance, Corro et al.[91] investigated the 3D stress distribution state along the c-axis of 6H-SiC under stress of 3.7 GPa, revealing through Raman spectroscopy that stress decreases exponentially with depth. To further understand the Raman-stress relation in SiC crystals, Onda et al.[92] conducted experiments to determine the relationship between stress in 4H-SiC and 6H-SiC crystals and the frequency shift in Raman spectroscopy. They employed a four-point bending test and performed Raman spectroscopy on single-crystal planes (size 5×5×45 mm), as shown in **Figure** 11a. The Raman spectrum of the 4H-SiC (0001) plane is shown in Figure 11b. Their analysis of the E_2 mode Raman shifts for both (0001) and (11–20) planes indicated that the Raman shifts decrease linearly with applied tensile stress, resulting in Raman shift-stress coefficients of

 © 2024 Wiley-VCH GmbH

18638899, 2024, 7, Downloaded from https://onlinelibrary.wiley.com/doi/10.1002/lpor.202301300 by Tu Delft, Wiley Online Library on [15/07/2024]. See the Terms and Conditions (https://onlinelibrary.wiley.com/terms-and-conditions) on Wiley Online Library for rules of use; OA articles are governed by the applicable Creative Commons License

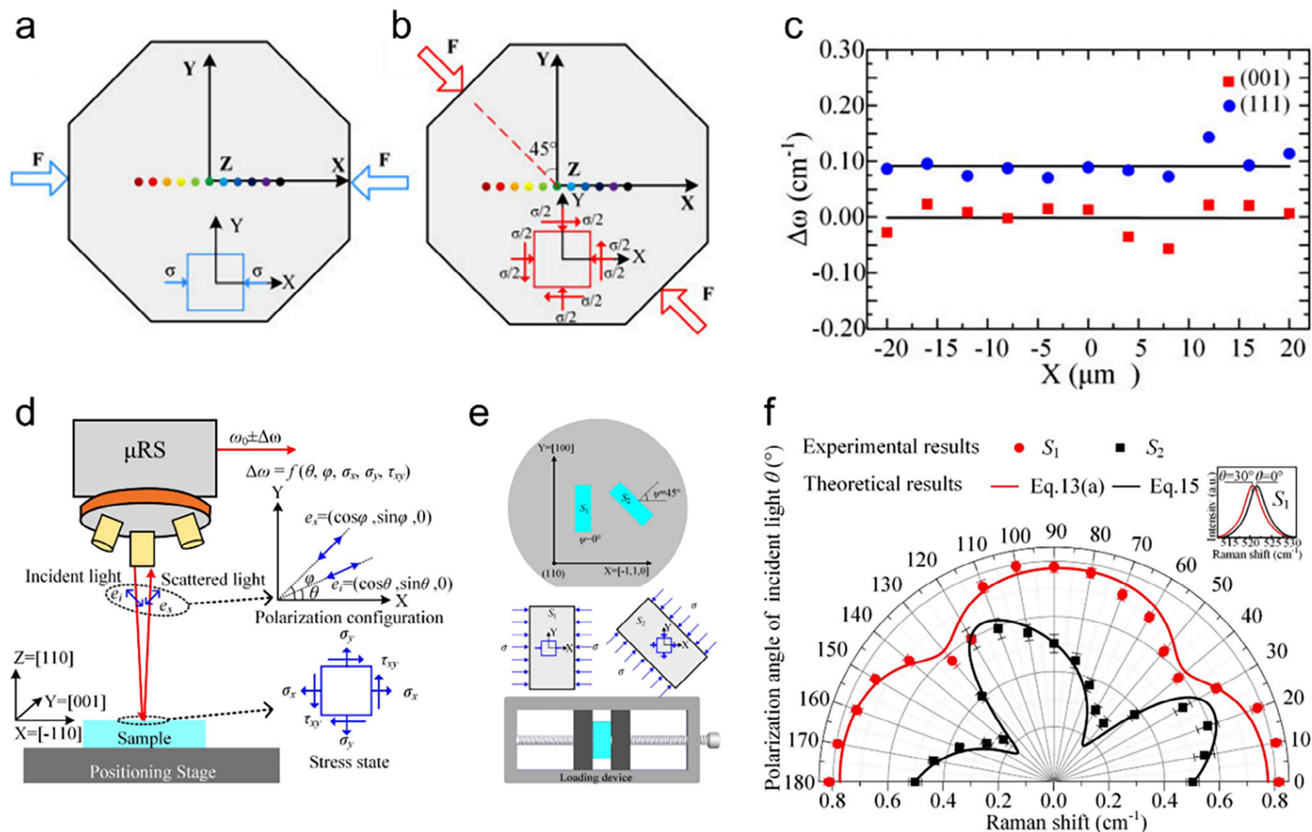

Figure 10. Schematic of stress loading experiment: a) uniaxial loading along X-axis and b) uniaxial loading along 45° direction. c) Measured experimental results. d) Schematic of Raman spectrum measuring plane stress state of Si surface with polarized device. e) Schematic of sample stress loading conditions. f) Comparison of experimental results of Raman wavenumber shift against theoretical prediction (θ from 0° to 180°) for S_1 and S_2. (a-c) Reproduced with permission.[89] Copyright 2018, IOP Publishing. (d-f) Reproduced with permission.[71] Copyright 2019, The Optical Society.

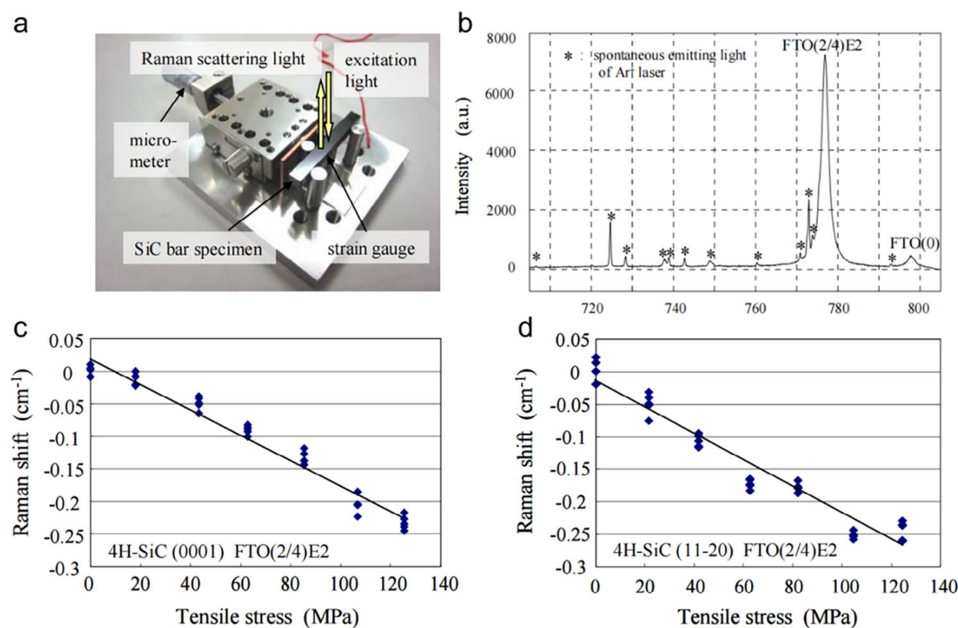

Figure 11. Experimental investigation of external stress loading of SiC and the Raman shift-stress relationship. a) Experimental setup for applying uniaxial stress to SiC square bar specimen under measuring Raman shift. b) Raman spectrum of 4H-SiC (0001) face. Correlation between tensile stress and Raman shift in 4H-SiC crystal: c) experimental results of 4H-SiC (0001) FTO(2/4)E_2 and d) experimental results of 4H-SiC (11–20) FTO(2/4)E_2. Reproduced with permission.[92] Copyright 2014, Springer Nature.

© 2024 Wiley-VCH GmbH

18638899, 2024, 7, Downloaded from https://onlinelibrary.wiley.com/doi/10.1002/lpor.202301300 by Tu Delft, Wiley Online Library on [15/07/2024]. See the Terms and Conditions (https://onlinelibrary.wiley.com/terms-and-conditions) on Wiley Online Library for rules of use; OA articles are governed by the applicable Creative Commons License

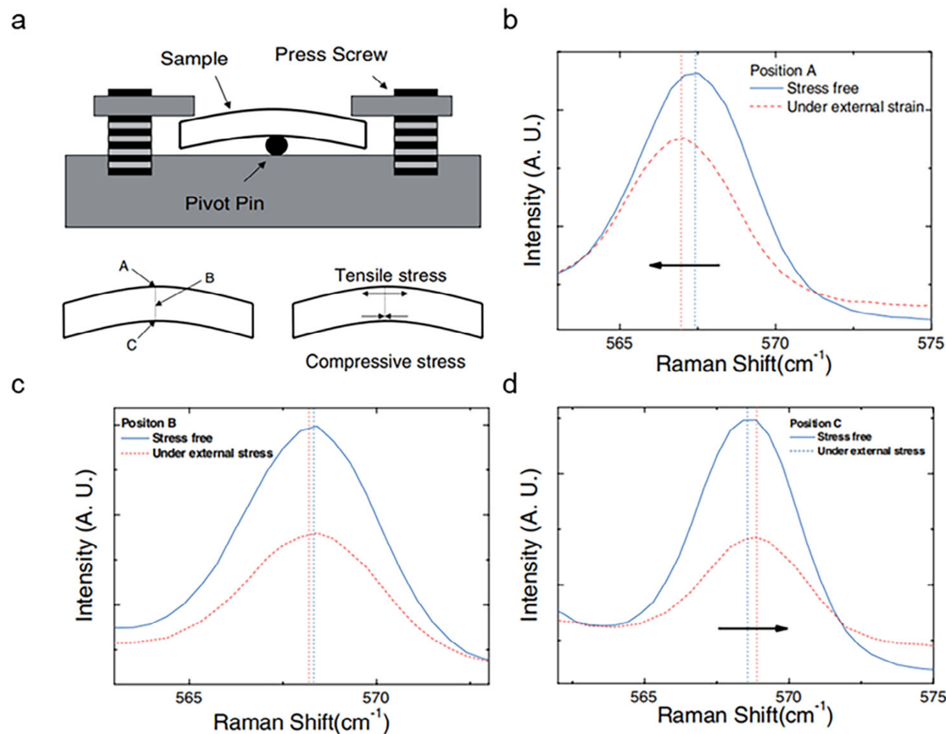

Figure 12. GaN Raman shift measurement under external stress and detection of stress distribution. a) Schematic of the device for applying external strain, position to be measured, and direction of stress during bending. Raman shift at Position b) A, c) B, and d) C with/without external strain. Reproduced with permission.[98] Copyright 2006, John Wiley and Sons.

−1.96 and −2.08 cm^{-1} GPa^{-1} for the (0001) and (11–20) planes, respectively (Figure 11c,d). Similarly, they found the Raman shift-stress coefficients for the (0001) and (11–20) planes of 6H-SiC crystals to be −2.70 and −1.30 cm^{-1} GPa^{-1}, respectively. This research lays a crucial groundwork for further advancements in Raman-based stress detection in SiC.

Addressing the influences of external damage on stress distribution, Tomar et al.[93] investigated the impact of ion irradiation and corrosion on SiC stress distribution. Using nanoindentation to measure local mechanical properties, they established a finite element method (FEM) model to predict stress distribution in SiC materials. Zhang et al.[94] conducted an extensive investigation into the influence of single-pulse femtosecond laser processing on the structural transformation and residual stress in 4H-SiC, including how laser flux affects residual stress.

6.1.3. Gallium Nitride (GaN)

GaN, recognized for its suitability as a substrate material for high-power, high-frequency, high-temperature, and optoelectronic semiconductor devices,[95–97] owes its preference to its wide direct bandgap (≈3.4 eV), high electron mobility, low impurity concentration, excellent electrical properties, exceptional thermal stability, and high conductivity. Consequently, measuring and analyzing residual stress in GaN materials has garnered increasing interest. In 2006, Kim et al.[98] researched the Raman spectrum of bulk GaN material under external bending stress conditions, as shown in **Figure 12a**. Their results tensile stress of ≈73 MPa (red-shift, $\Delta\omega$ is −0.45 cm^{-1}) at the top of the bulk GaN template and compressive stress of ≈40 MPa, (blue-shift, $\Delta\omega$ is 0.25 cm^{-1}) at the bottom, as shown in Figure 12b–d. This investigation establishes a critical foundation for exploring the relationship between optical properties and internal stress in GaN materials.

The pursuit of low-stress GaN crystals is significantly driven by advancements in epitaxy or deposition techniques, emphasizing the need for an in-depth exploration of how growth conditions affect stress distribution. Lee et al.[99] utilized gradient V/III ratio technology to grow high-quality bulk GaN with a thickness of 3.5 mm, as shown in **Figure 13a**. Raman spectroscopy analysis revealed that the peak position of the E_2 mode in the bulk GaN crystals decreased with a reduction in the V/III ratio, a trend observed across conditions I, II, and III (Figure 13b). Compared to unstressed GaN, all samples exhibited a red-shift, with residual tensile stresses of ≈0.70, 0.37, and 0.47 GPa, respectively.

Furthermore, the research on GaN processing properties is important. Nanoindentation is recognized as an effective method for exploring material processing properties at micro- and nanoscales. Leveraging this method, Qiu et al.[35] explored the in-plane residual stress components around a Berkovich indentation on the (0001) plane of GaN using polarization Raman spectroscopy. Their experiments uncovered significant differences in stress component distribution compared to Raman shift distribution closely linked to GaN crystal structure and exhibiting a gradient along each crystal direction. The distribution of the E_2 mode

© 2024 Wiley-VCH GmbH

18638899, 2024, 7, Downloaded from https://onlinelibrary.wiley.com/doi/10.1002/lpor.202301300 by Tu Delft, Wiley Online Library on [15/07/2024]. See the Terms and Conditions (https://onlinelibrary.wiley.com/terms-and-conditions) on Wiley Online Library for rules of use; OA articles are governed by the applicable Creative Commons License

18638899, 2024, 7, Downloaded from https://onlinelibrary.wiley.com/doi/10.1002/lpor.202301300 by Tu Delft, Wiley Online Library on [15/07/2024]. See the Terms and Conditions (https://onlinelibrary.wiley.com/terms-and-conditions) on Wiley Online Library for rules of use; OA articles are governed by the applicable Creative Commons License

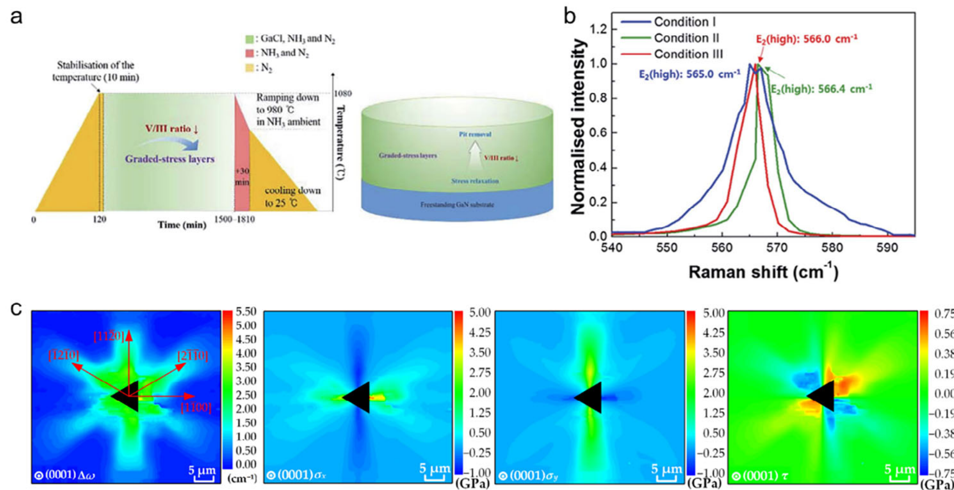

Figure 13. Detection of Raman shifts during growth and stress evolution in nanoindentation regions. a) Schematic of GaN growth process. b) Raman spectra of GaN grown with different V/III ratios. c) E_2 mode Raman shift map on (0001) plane, as well as distribution of normal stress σ_x, σ_y, and shear stress τ_{xy}. (a,b) Reproduced under terms of CC-BY 3.0 license.[99] Copyright 2018, The Authors, published by The Royal Society of Chemistry. (c) Reproduced under terms of CC-BY 4.0 license.[35] Copyright 2023, The Authors, published by MDPI.

Raman displacement on the (0001) plane around the indentation, as shown in Figure 13c, highlights an area of increased displacement near the indentation, indicating compressive-stress dominance in the residual stress field. The Raman shift increased along the, [2–1–10], [11–20], and [−12–10] directions at the center of the indentation, and decreased with distance from the center. The Raman spectrum decayed more slowly along the [2–1–10] and [−12–10] directions and more quickly along the [11–20] direction. Specifically, σ_x exhibited positive values along the, [2–1–10] [−12–10], and [1–100] directions, and negative values along the [11–20] direction, while σ_y was positive along the, [2–1–10] [−12–10], and [11–20] directions, and negative along the [1–100] direction. Near the indentation's edge, σ_x and σ_y primarily aligned with the [1–100] and [11–20] directions, respectively, whereas at the far end of the indentation, they predominantly aligned along the, [2–1–10], [11–20] and [−12–10] directions. Based on stress distribution characteristics, the 2 stress components were symmetric along the [1–100] and [11–20] directions, with the shear stress showing both positive and negative values.

6.1.4. Sapphire (Al_2O_3)

Sapphire (Al_2O_3) substrates offer numerous advantages, including high thermal conductivity, exceptional transparency, physical and chemical stability, excellent electrical insulation, and strong mechanical strength. These substrates are increasingly used in LEDs and other optoelectronic devices, highlighting their significance in the field.

The processing of Al_2O_3 poses challenges due to its high hardness and brittleness, with conventional techniques often leading to stress-related problems such as cracks, fractures, and surface damage. To address these issues, Mann et al.[100] introduced Micro-Laser Assisted Machining (μ-LAM) as a solution to the significant stress issues encountered with traditional sapphire processing techniques, as shown in **Figure** 14a. Micro-Raman spectroscopy was utilized to quantify the residual stress induced by this technology. The stress distribution in sapphire subjected to μ-LAM technology, illustrated in Figure 14b, reveals a compressive-stress zone both within and along the edge of the cut, spanning ≈2–3 μm in width with a uniform stress distribution. Moving away from the cut, the stress rapidly transitions from compressive to tensile stress with a 1–2 μm range, with the highest tensile stress located ≈5 μm from the center of the cut. This research indicated that laser-assisted processing can effectively mitigate residual stress, reducing the occurrence of fractures, cracks, and chipping in sapphire. The investigation into the residual stress on various sapphire crystal faces during processing has garnered significant interest due to the material's anisotropic nature. For instance, Min et al.[101] employed micro-Raman spectroscopy to investigate the anisotropy of residual stress resulting from ultraprecision machining on 2 crystal planes of sapphire. Figure 14c illustrates the equivalent residual stress on R-plane, showing predominantly tensile stress except in the brittle region of the 90° cut, with stress magnitudes varying significantly with the cutting direction. For the 150° cutting direction, residual stress ranged from tens to 150 MPa, decreasing with increased cutting depth as stress was relieved through crack formation. Conversely, the 180° cutting direction showed the most significant residual stress in the brittle region. Figure 14d shows the equivalent residual stress on C-plane, which, unlike the R-plane, was negligible and uniform across various cutting directions. These results reveal that residual stress varies across different crystal planes and is influenced by the cutting direction during machining.

In summary, the precise measurement and understanding of internal stress in substrate materials represent a dynamic field requiring continuous advancements and refinements. These advancements are crucial for uncovering the origins of stress in semiconductor materials and optimizing material production processes, offering invaluable insights into the semiconductor industry.

 © 2024 Wiley-VCH GmbH

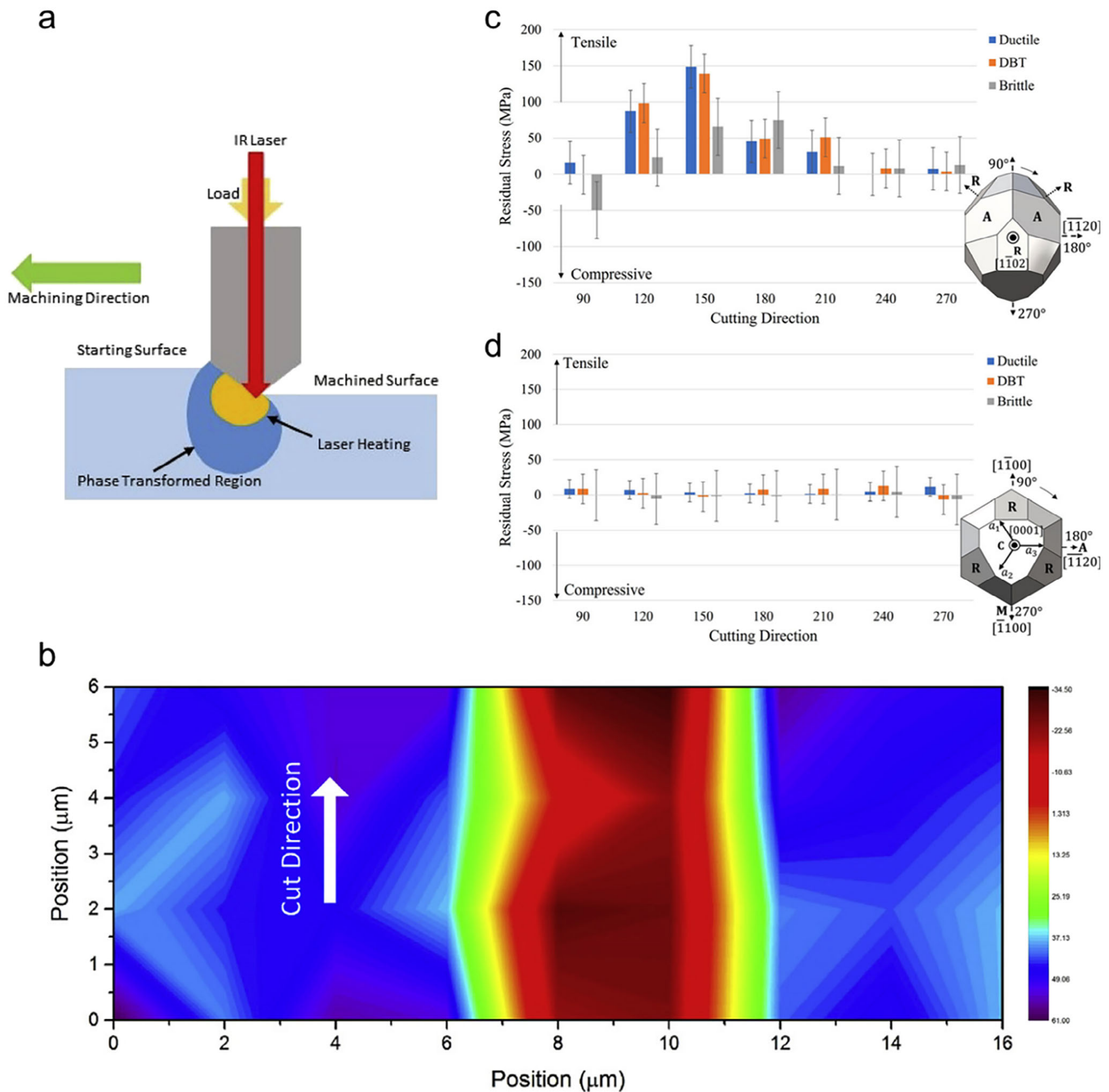

Figure 14. Machining process and Raman-stress measurement of sapphire. a) Schematic of μ-LAM process; b) Stress profile of sapphire processed using μ-LAM technology with thrust/applied force of 20 mN, low-power laser assistance, a diamond tip with a radius of 5 μm, and nominal cutting depth of ≈100 nm. The unit of stress is MPa. c) Residual stresses in various cutting directions on R-plane of the sapphire. d) Residual stresses in various cutting directions on C-plane of the sapphire. (a,b) Reproduced with permission.[100] Copyright 2019, Elsevier. (c,d) Reproduced with permission.[101] Copyright 2022, Elsevier.

6.2. Epitaxial Thin Film

With the rapid growth of the electronics industry, the demand for advanced semiconductor materials has significantly increased. Epitaxial semiconductor thin films, in particular, are pivotal for the development of high-performance devices. However, stress within these epitaxial films has become a major concern due to its potential impact on material properties and device performance.[102] The primary stress sources in these films include lattice mismatch between the epitaxial film and the substrate, differences in thermal expansion coefficients, and defect density.[103–105] In response, there are ongoing efforts to optimize and develop innovative thin-film epitaxy processes aimed at minimizing the residual stress induced by these factors.

18638899, 2024, 7, Downloaded from https://onlinelibrary.wiley.com/doi/10.1002/lpor.202301300 by Tu Delft, Wiley Online Library on [15/07/2024]. See the Terms and Conditions (https://onlinelibrary.wiley.com/terms-and-conditions) on Wiley Online Library for rules of use; OA articles are governed by the applicable Creative Commons License

Techniques under exploration include migration-enhanced metal-organic chemical vapor deposition,[106,107] growth mode alternating multilayer technology,[108–110] selective chemical vapor deposition,[111,112] and molecular beam epitaxy.[113,114] To facilitate the production of high-quality epitaxial films with minimal residual stress, accurately characterizing these films' residual stress and understanding stress evolution during growth are crucial. Such investigation provides valuable insights into refining epitaxial film production processes.

6.2.1. Diamond Film

Diamond thin films have garnered significant interest due to their exceptional optical, electrical, and mechanical properties,[115,116] making them highly promising for various applications in optical, photonic, and electronic devices.

Atomic doping of diamond films, a common modification method, can introduce lattice distortion and residual stress. Therefore, the impact of doping on stress distribution in diamond films is a focal point of research. For instance, Mermoux et al.[117] investigated the stress profile of homoepitaxial (111)-oriented phosphorus-doped diamond films, observing that the epitaxial layer signal (1326 cm^{-1}) weakened with increasing focal depth, while the diamond substrate signal (1332 cm^{-1}) strengthened. The epitaxial film surface exhibited the highest tensile stress, which rapidly diminished to zero with depth before transitioning into compressive-stress, suggesting that the interface primarily experiences compressive-stress. Moreover, the size of the epitaxial diamond film on the substrate significantly influences the stress at the film's edge. Holtz et al.[118] utilized ultraviolet (363.8 nm) micro-Raman stress mapping to examine the selective growth of diamond stripes on the Si substrates with different widths and an average thickness of ≈1.5 μm (**Figure 15**a–d). The internal stress distribution varied with stripe width (20, 40, 80 μm) are shown in Figure 15e,f, with the maximum shift (compressive-stress) concentrated near the center of each stripe and decreasing toward the edges. For Si substrates, lower tensile stresses were observed beneath the diamond, with increased compressive stresses at the fringe edges. The diamond's compressive-stress decreased as the stripe width narrowed.

Beyond investigating stress in epitaxially grown diamond films, understanding the impact of processing techniques on the stress distribution within these films is essential. Bendavid et al.[119] proposed a novel approach to customize the stress properties of diamond films through boron doping and focused ion beam milling for microbridge microfabrication (**Figure 16**a,b). They studied the resultant stress distribution using detailed confocal micro-Raman spectroscopy. Figure 16c shows the numerical stress distribution ($\sigma_{xx} + \sigma_{yy}$) within microbridge 1 (MB1), revealing significant variation across different areas of MB1, with stress peaking at 1.74 GPa in the bridge (B) region and decreasing to 0.96 ± 0.07 GPa in the left (PL) and right pads (PR), compared to an average stress of 1.1 GPa in nonpatterned areas. Similarly, Figure 16d presents the stress ($\sigma_{xx} + \sigma_{yy}$) distribution for microbridge 2 (MB2), where the absence of rectangular pads PL and PR notably influenced the ($\sigma_{xx} + \sigma_{yy}$) distribution. The average stress in the left triangular (TL) and right triangular (TR) pad regions was slightly lower than in the nonpatterned region (1.70 GPa), while the stress of the B region was significantly reduced to 1.31 ± 0.04 GPa. These results demonstrate that stress in the boron-doped diamond/diamond layer could be modulated through appropriate microbridge geometry and boron doping.

6.2.2. Silicon Carbide (SiC) Film

SiC thin films are recognized for their excellent high-temperature stability, high electron mobility, low electron drift, and wide-bandgap,[120] making them suitable for high-temperature, high-frequency, high-voltage, and high-power applications.

Research on stress distribution in SiC epitaxial films has primarily focused on the 3C-SiC phase. Lee et al.[77] employed chemical vapor deposition (CVD) to selectively grow a 3C-SiC film with a low interface defect density on a Si (111) substrate, employing Raman spectroscopy to assess the residual stress field at the interface. The results showed a consistent presence of tensile stress between the epitaxial film and the silicon substrate. Pezzotti et al.[121] explored the stress effects associated with different crystal plane orientations of silicon substrates on the epitaxy of 3C-SiC films through Raman spectroscopy, concluding that high-quality cubic silicon carbide single crystals could be obtained on silicon substrates irrespective of orientation. Moreover, the stress distribution in 3C-SiC thin films influenced by Si substrate surface defects has attracted research interest. Grudinkin et al.[122] examined the effects of voids in Si substrates on stress distribution in 3C-SiC thin films during CVD growth. Their results confirmed that 3C-SiC films epitaxially grown on Si substrates predominantly exhibited tensile stress, aligning with prior findings. Additionally, stress levels outside the voids exceeded those inside, indicating that cavities contributed to stress relief.

Other studies have delved into how growth rate,[123] epitaxial thickness,[124] and doping[123,125] affect the stress in 3C-SiC films.

6.2.3. Gallium Nitride (GaN) Film

GaN thin films, alongside SiC, stand as significant examples of third-generation semiconductors, attracting considerable research focus.[126–129] Therefore, comprehensive wafer-wide epitaxial stress characterization has become pivotal in the study of stress in GaN thin films. Holtz et al.[130] investigated the stress of GaN films epitaxially grown on diamond substrates utilizing Raman spectroscopy (**Figure 17**a,b). By employing both visible light and ultraviolet Raman spectroscopy, they were able to visually map the stress distribution across the entire wafer. Figure 17c,d illustrates that the epitaxial thin-film GaN generally exhibits tensile stress. However, there is a notable difference in stress distribution from the upper to the lower sides of the films, with a gradient distribution (ranging from 1.0 to 0.075 GPa) observed from the surface down to the bottom interface.

While nanoindentation is a relatively straightforward technique for studying the mechanical properties of bulk GaN,

 © 2024 Wiley-VCH GmbH

18638899, 2024, 7, Downloaded from https://onlinelibrary.wiley.com/doi/10.1002/lpor.202301300 by Tu Delft, Wiley Online Library on [15/07/2024]. See the Terms and Conditions (https://onlinelibrary.wiley.com/terms-and-conditions) on Wiley Online Library for rules of use; OA articles are governed by the applicable Creative Commons License

18638899, 2024, 7, Downloaded from https://onlinelibrary.wiley.com/doi/10.1002/lpor.202301300 by Tu Delft, Wiley Online Library on [15/07/2024]. See the Terms and Conditions (https://onlinelibrary.wiley.com/terms-and-conditions) on Wiley Online Library for rules of use; OA articles are governed by the applicable Creative Commons License

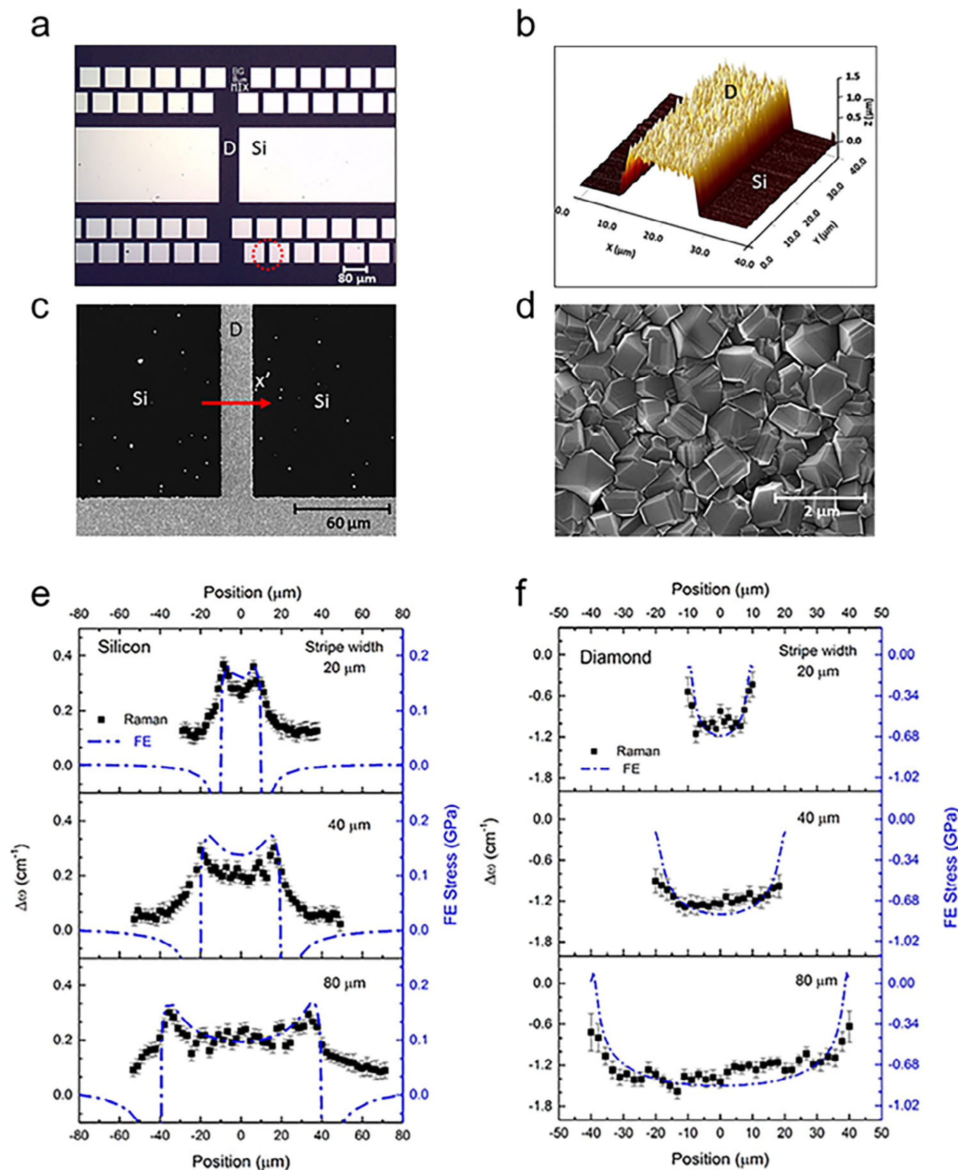

Figure 15. Research on stress distribution of epitaxial diamond films under different sizes. a) Optical image of the grown diamond. b) AFM image of 20 µm wide diamond stripe. c) SEM images of 20 µm wide diamond stripes and silicon substrates. d) High magnification SEM image of epitaxial diamond film. Comparison of Raman measured and theoretical stress maps for e) Si substrates and f) diamond. Stripe width: 20, 40 and 80 µm. Reproduced with permission.[118] Copyright 2018, AIP Publishing.

applying it to nanofilms is challenging due to the significant influence of the substrate on indenter behavior, which complicates the isolation of signals directly from the film. Addressing this, Redkov et al.[131] investigated the nanoindentation characteristics of epitaxial GaN films on SiC buffer layers atop Si substrates utilizing confocal Raman spectroscopy. They detailed the mechanical stress distribution and crystal quality (based on FWHM) of GaN and Si near the indenter at different indentation depths and investigated the anisotropy of elastic stress propagation during indentation. **Figure** 18a demonstrates that at a low pressure of 50 mN, the mechanical stress propagation showed significant anisotropy, influenced by the material's crystallographic orientation and the relative orientation between the indenters. Beyond 200 mN, the stress propagation in the GaN film became radially symmetric, showing less dependence on a direction. At 500 mN, a clear separation between the film and substrate was observed in the indentation region, concentrating the original mechanical stress nearby before it sharply decreased to zero with distance. The minimal stress in the Si substrate was mainly due to pores introduced during the growth of the SiC buffer layer, which facilitated stress relaxation nearby. Figure 18b delves deeper into the mechanical stress propagation and crystal quality along the depth of the Si substrate. The results clearly illustrate that both stress distribution within the silicon

 © 2024 Wiley-VCH GmbH

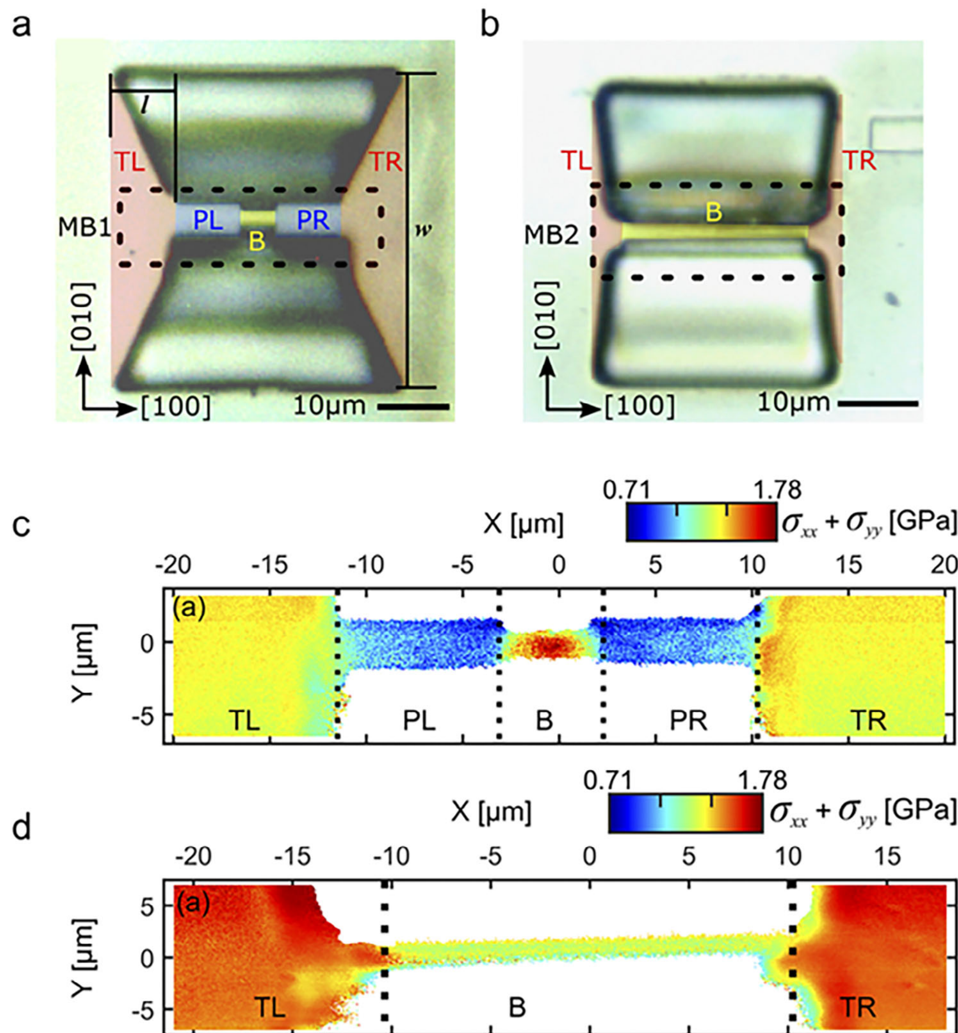

Figure 16. Stress distribution in microbridge-processed diamond films. Optical image of a) MB1 and b) MB2 structure. Raman-stress relation map of c) MB1 and d) MB2 structure ($\sigma_{xx} + \sigma_{yy}$). Reproduced under terms of CC-BY 4.0 license.[119] Copyright 2021, The Authors, published by AIP Publishing.

substrate and its FWHM are significantly influenced by the depth.

6.2.4. Aluminum Nitride (AlN) Film

Aluminum nitride (AlN) thin films are highly valued for their biocompatibility, high thermal conductivity, and excellent dielectric properties, making them suitable for a variety of applications.[132–136] Their thermal expansion coefficients closely align with those of silicon, potentially reducing the probability of thermal stress-induced failures in silicon-based devices. This has led to a surge in research on thin-film materials in recent years.

Research on the quality and stress distribution of AlN epitaxial films grown by different processes has become an important area of focus. Solonenko et al.[137] investigated epitaxial hexagonal AlN films on Si (111) substrates prepared through magnetron sputtering, particularly examining the effects of annealing on crystal quality via Raman spectroscopy. Analysis of the annealed AlN film (**Figure 19a**) indicated a shift in the Raman wavenumber to a lower frequency compared to unstressed AlN, indicating the presence of tensile stress with an estimated average stress of ≈0.6 GPa based on the Raman-stress factor value of −6.3 cm^{-1} GPa^{-1} for the E_2 mode. The position of the AlN mode during annealing, as shown in Figure 19b, was closely related to annealing temperature, with stress release observed up to 800 °C and a transition to the characteristic frequency range of strain-free AlN crystals at higher temperatures, indicating a potential relationship change at the AlN-Si interface ≈800 °C. Feng et al.[138] grew AlN films on 6H-SiC and Al_2O_3 substrates using metal-organic CVD and employed Raman scattering to explore the film stress and temperature relationship. The Raman spectrum of AlN/Al_2O_3 samples, excited at 532 nm (Figure 19c), showed a higher frequency shift in the E_2 mode, indicating compressive-stress, while AlN/6H-SiC samples exhibited a lower frequency shift, suggesting tensile stress. The observed shifts for AlN/Al_2O_3 and AlN/6H-SiC samples under unstressed conditions were −0.5 and −9.28 cm^{-1}, respectively (Figure 19d),

18638899, 2024, 7, Downloaded from https://onlinelibrary.wiley.com/doi/10.1002/lpor.202301300 by Tu Delft, Wiley Online Library on [15/07/2024]. See the Terms and Conditions (https://onlinelibrary.wiley.com/terms-and-conditions) on Wiley Online Library for rules of use; OA articles are governed by the applicable Creative Commons License

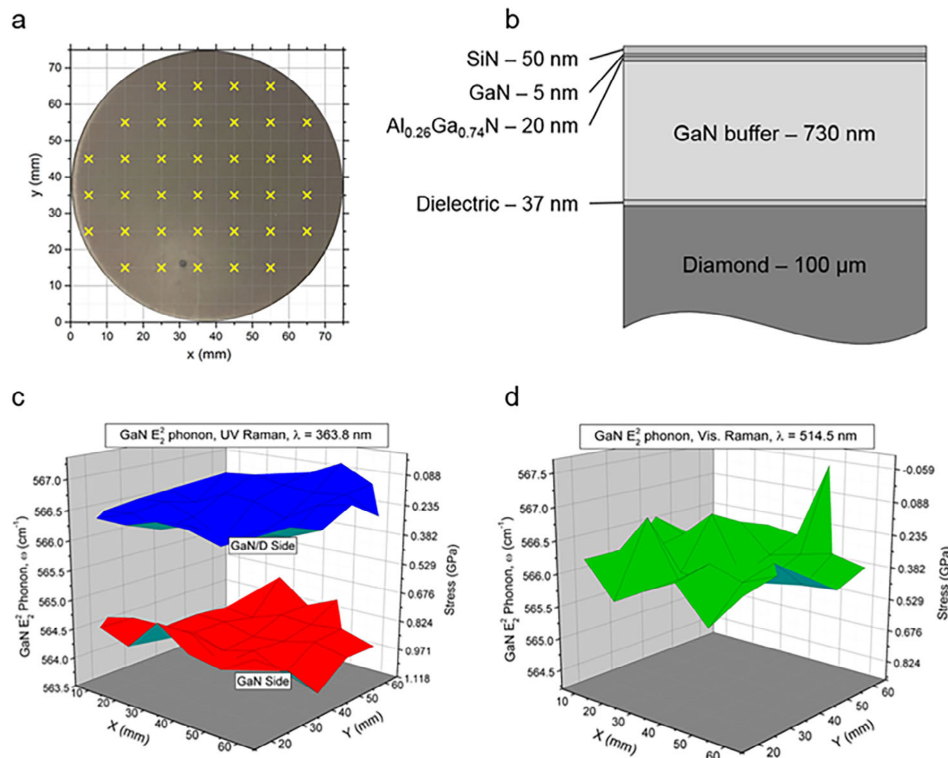

Figure 17. Growth stress full wafer inspection of epitaxial GaN films a) Coordinate system used for Raman-stress relation mapping in the wafer. b) Schematic of epitaxial layer structure. Raman measurement images of sample E_2 phonon mode: c) UV excitation and d) visible light excitation. Reproduced with permission.[130] Copyright 2016, AIP Publishing.

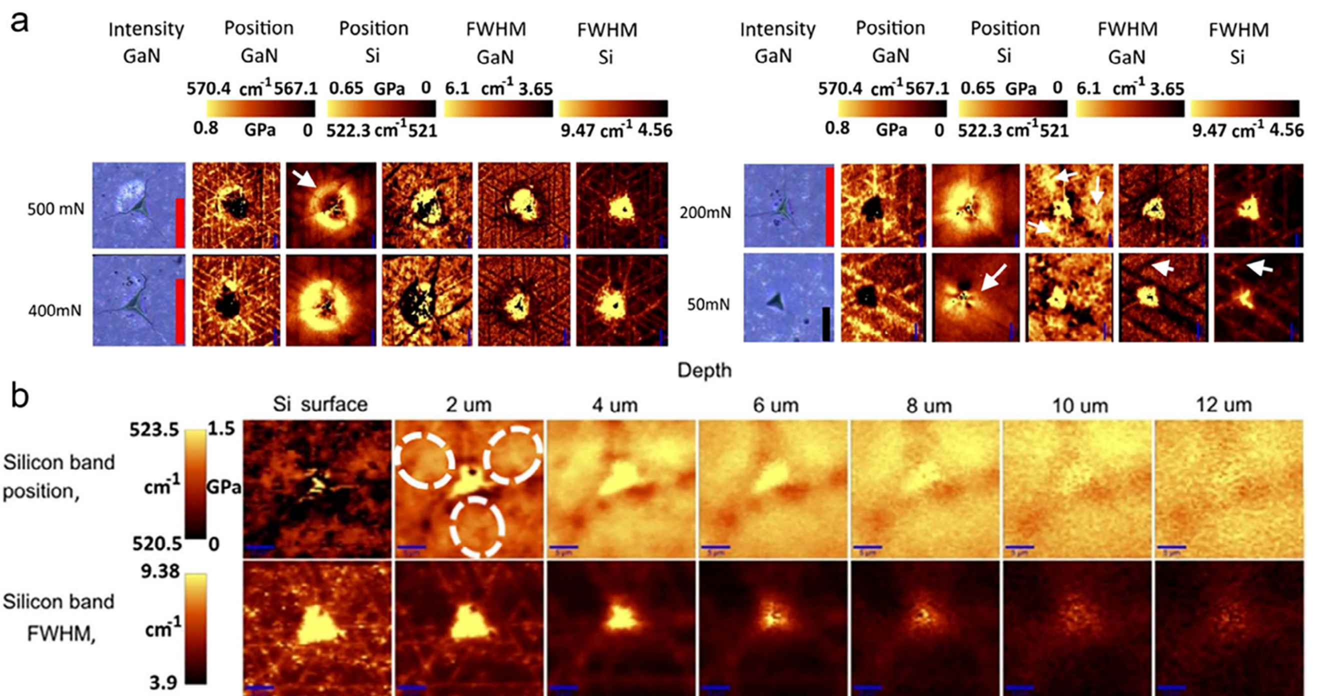

Figure 18. Stress distribution in nanoindentation region of epitaxial GaN films. a) Raman intensity, peak position, and FWHM test pattern of the Si substrate and GaN epitaxial layer under different pressures. b) Peak position and FWHM evolution with depth for Si substrate under 200 mN pressure. Reproduced with permission.[131] Copyright 2017, Elsevier.

18638899, 2024, 7, Downloaded from https://onlinelibrary.wiley.com/doi/10.1002/lpor.202301300 by Tu Delft, Wiley Online Library on [15/07/2024]. See the Terms and Conditions (https://onlinelibrary.wiley.com/terms-and-conditions) on Wiley Online Library for rules of use; OA articles are governed by the applicable Creative Commons License

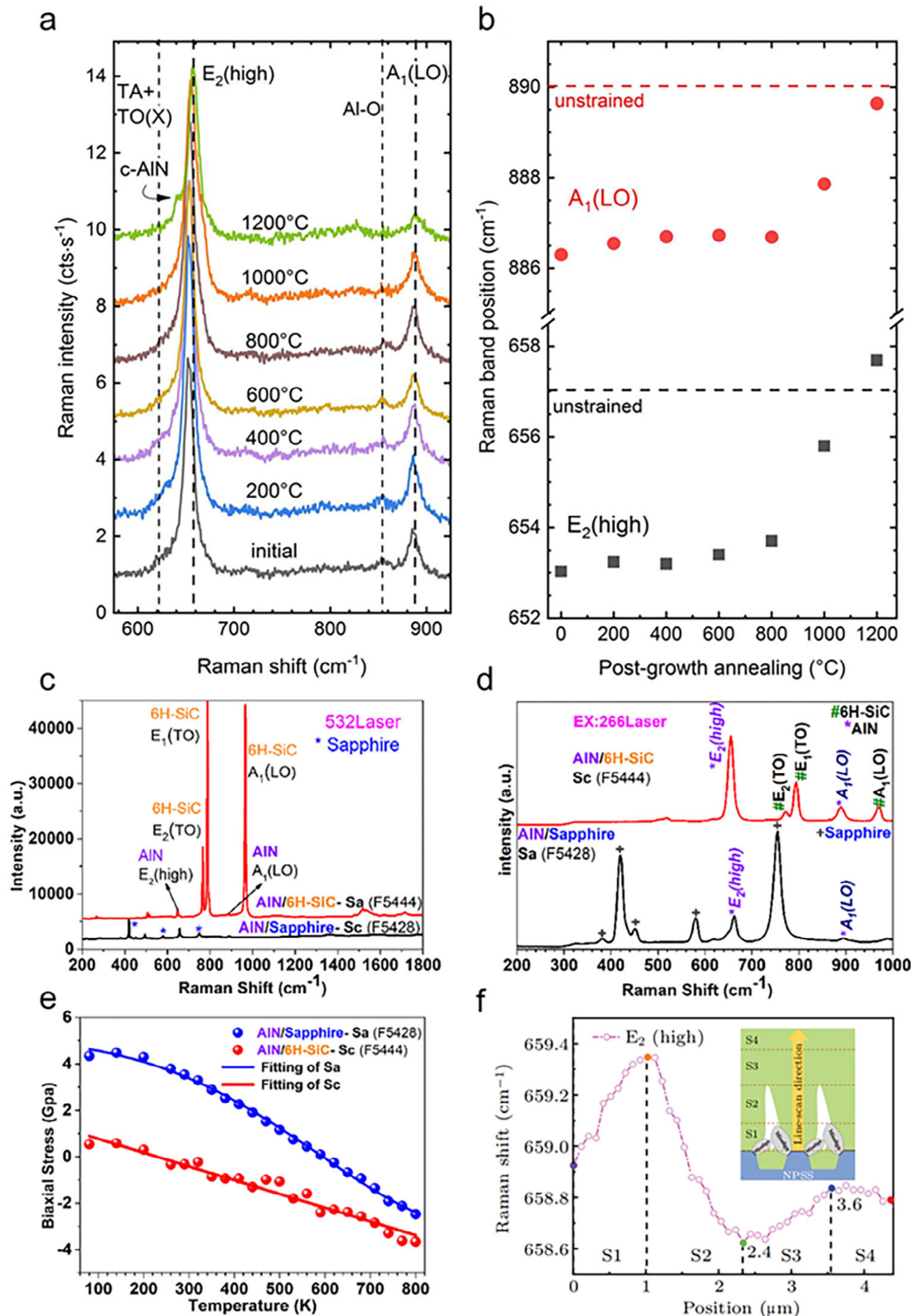

Figure 19. Stress-annealing temperature relationship of epitaxial AlN films and stress evolution during growth. a) Raman results of AlN/Si(111) samples after post-growth annealing. b) Relationship function between peak position of E_2 and A_1 phonon mode with post-growth annealing temperature. Raman spectra excited by c) 532 nm and d) 266 nm. e) Relationship function between stress in AlN film and temperature.f) The shift of the E_2 phonon mode peak along the growth direction. (a,b) Reproduced with permission.[137] Copyright 2019, John Wiley and Sons. (c-e) Reproduced with permission.[138] Copyright 2021, Elsevier. (f) Reproduced with permission.[139] Copyright 2023, IOP Publishing.

© 2024 Wiley-VCH GmbH

18638899, 2024, 7, Downloaded from https://onlinelibrary.wiley.com/doi/10.1002/lpor.202301300 by Tu Delft, Wiley Online Library on [15/07/2024]. See the Terms and Conditions (https://onlinelibrary.wiley.com/terms-and-conditions) on Wiley Online Library for rules of use; OA articles are governed by the applicable Creative Commons License

attributed to thermal expansion coefficient mismatches between the films and substrates. The film stress change curve with temperature for both sample types revealed varying stress behaviors, with AlN/Al_2O_3 samples, transitioning from compressive to tensile stress within the 600–800 K range and continuing to increase with temperature, as shown in Figure 19e. While AlN/6H-SiC samples showed a decrease in compressive-stress within the 80–250 K range before transitioning to tensile stress. Subsequently, the compressive-stress in the AlN film transitioned to tensile stress, which gradually increased as the temperature rose. This comparison revealed that the temperature at which the stress undergoes an abrupt change for the Al_2O_3 substrate (600 K) is higher than that for the 6H-SiC substrate (250 K), a discrepancy due to the differences in thermal expansion coefficients among the 3 materials. Xu et al.[139] utilized hydride vapor phase epitaxy to grow a crack-free AlN film on a 4-inch hole-shaped nanopatterned sapphire substrate, investigating the stress evolution law with film thickness through cross-sectional Raman line scanning (Figure 19f). The Raman frequency of the E_2 mode varied significantly along the growth direction, indicating overall compressive-stress within the film as a whole (stress-free peak position: 657.4 cm^{-1}). These fluctuations were divided into 4 stages (S1–S4), with the peak compressive-stress near the interface at a depth of 1 µm in the S1 stage, attributed to the thermal expansion coefficient mismatch between AlN and sapphire and early growth stage competitions. The frequency decreased gradually with layer coalescence in the S2 stage, and a slight increase in stress was noted in the S3 stage, likely due to misorientation in regions adjacent to the coalescence region.

In summary, stress in semiconductor epitaxial films plays a dual role in device performance. Strategic stress engineering can enhance electronic device performance by fine-tuning epitaxial growth conditions to optimize carrier mobility, bandgap energy, and device functionality for specific applications. Conversely, excessive stress in epitaxial films can detract from device performance and reliability, leading to issues such as dislocations, cracks, reduced carrier mobility, increased leakage current, and diminished device lifespan. Therefore, identifying and addressing stress-induced defects is crucial for the long-term performance and reliability of semiconductor devices.

6.3. Patterning

Semiconductor patterning techniques play an important role in modern electronics, directly affecting material properties and device performance, with stress being a crucial factor affected by patterning. Understanding the impact of patterning on stress is essential for optimizing device design and reliability.

Recognizing that accumulated residual stress can lead to crack formation, Hossain et al.[140] utilized Raman spectroscopy to examine the stress distribution in GaN thin films on patterned Si substrates with various mesa sizes, trench heights, and trench widths. They conducted linear Raman scans along the long diagonal axis of the rhomboid mesa (400 µm) and utilized the biaxial plane stress model and E_2 mode to calculate the GaN stress variation (**Figure** 20a). The findings revealed a symmetric distribution of tensile stress, peaking at the rhombus's center (1.8 GPa) and exhibiting a consistent U-shaped stress distribution trend across different mesa sizes (Figure 20b). Moreover, the maximum center stress increased with mesa size. In the (110) crystal plane of the patterned 200 µm mesa Si substrate, Figure 20c demonstrated the E_2 peak shift of GaN at different groove heights (5, 10, 15 µm) suggesting that maintaining the trench height above the GaN thickness (12 µm) significantly reduced residual stress, while the groove width minimally impacted it (Figure 20d). However, the study faced statistical limitations due to the randomness in crack generation. Therefore, further research based on statistics in subsequent studies was conducted.[141] The results (Figure 20e) revealed that the percentage of fractured mesas increased with mesa size, with in-plane stress nearing 1.8 GPa for mesas larger than 100 µm (Figure 20f). Variations in in-plane stress for 400 µm mesas were linked to differences in the growth at film edges or depths. Additionally, deeper trench heights (15 µm) resulted in reduced mesa stress compared to 5 and 10 µm heights, demonstrating significant stress alleviation with increased trench height. Conversely, variations in trench widths (Figure 20g,h) did not significantly affect the percentage of fractured mesas or in-plane stress, indicating that cracks and in-plane stress are nearly independent of trench width.

Beyond this focused patterned stress research, Griffin et al.[142] explored local stress changes in AlN after patterned metallization using a planar biaxial stress model (**Figure 21**a). The transition region from plasma-enhanced tetraethylorthosilicate (PETEOS) to the bottom metal exhibited a notable tensile shift in AlN residual stress compared to the stress on the PETEOS/Si substrate (Figure 21b,c), indicating an inhomogeneous stress distribution within the AlN/metal/PETEOS/Si wafer (Figure 21d).

Semiconductor patterning technology is pivotal in contemporary electronic device fabrication, yet the residual stress it induces significantly influences device performance and reliability. While current research in this domain has made notable outcomes, continued in-depth exploration is imperative to drive semiconductor patterning technology forward, leading to substantial advancements in device design and reliability enhancement.

6.4. Interconnections in Packaging

The surge in demand for portable and wireless electronic devices has propelled the need for high-density integrated-circuit (IC) technology, spurring the development of new interconnect technologies. As we strive for higher integration levels, understanding the impact of interconnection techniques on the residual internal stresses of semiconductor devices becomes crucial. Various interconnection technologies, including wire bonding, flip chips, and through-silicon vias (TSVs), introduce varying residual stress distributions in these devices. Therefore, investigating the residual stress resulting from actual interconnection processes, considering changes in stress/strain layers, and utilizing stress characterization techniques to assess their potential effects on the long-term performance of microelectronic devices are critical steps.

6.4.1. Die Attach

The adhesive fixation between the chip and substrate is a crucial step in establishing electrical and mechanical connections,

© 2024 Wiley-VCH GmbH

18638899, 2024, 7, Downloaded from https://onlinelibrary.wiley.com/doi/10.1002/lpor.202301300 by Tu Delft, Wiley Online Library on [15/07/2024]. See the Terms and Conditions (https://onlinelibrary.wiley.com/terms-and-conditions) on Wiley Online Library for rules of use; OA articles are governed by the applicable Creative Commons License

18638899, 2024, 7, Downloaded from https://onlinelibrary.wiley.com/doi/10.1002/lpor.202301300 by Tu Delft, Wiley Online Library on [15/07/2024]. See the Terms and Conditions (https://onlinelibrary.wiley.com/terms-and-conditions) on Wiley Online Library for rules of use; OA articles are governed by the applicable Creative Commons License

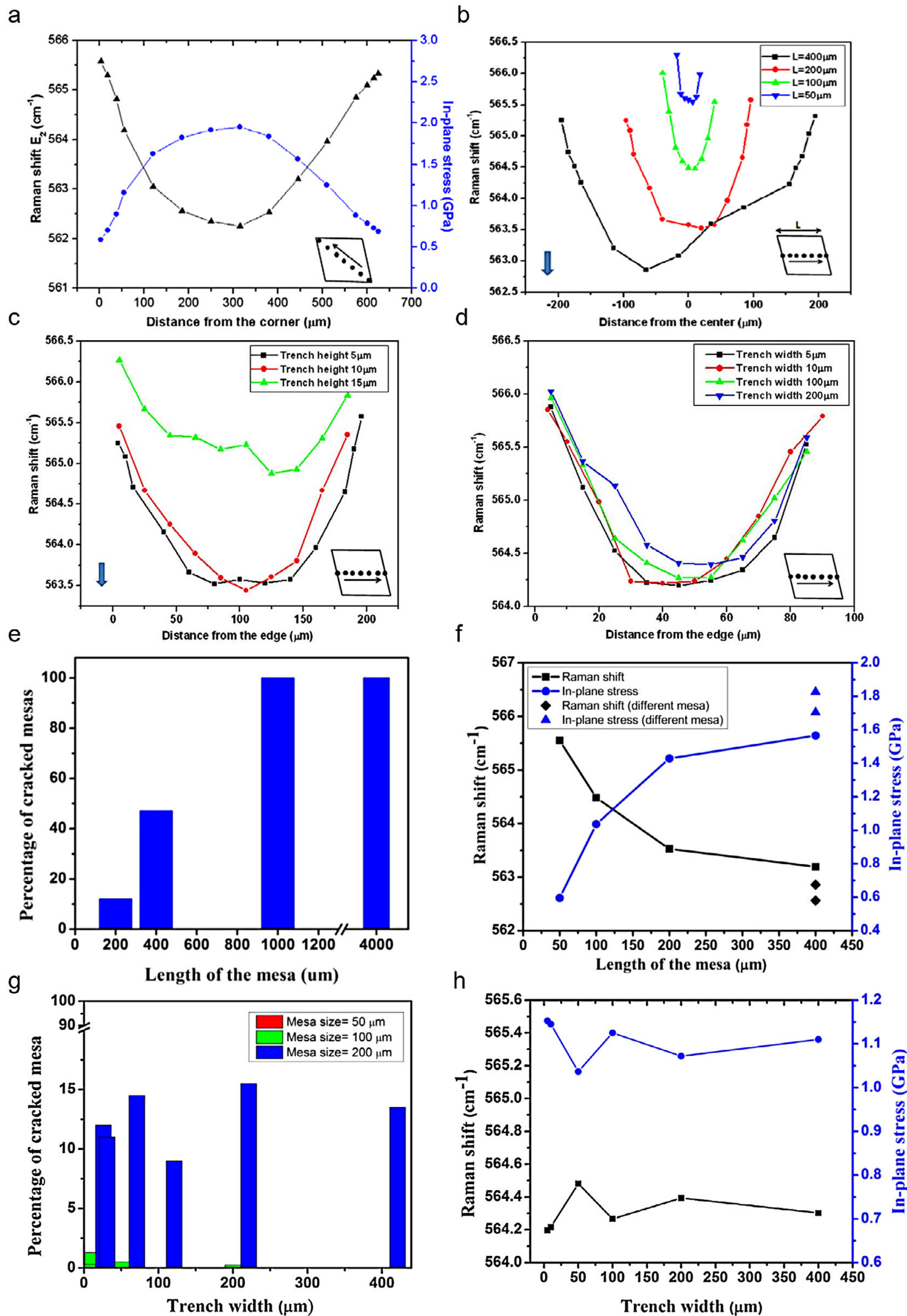

Figure 20. Effect of the surface patterning process for internal stresses in GaN. a) Raman shift and in-plane stress distribution of long diagonal axis of rhombohedral GaN (400 μm) grown on patterned Si (110). b) Raman shifts of E_2 phonon modes of rhombohedral GaN with different sizes. Raman shifts of E_2 phonon modes of rhombic GaN mesas (200 μm) at different c) trench heights and d) trench widths. e) Percentage of ruptured mesas. f) Raman shift and in-plane stress plots of crack-free mesa with different sizes. g) Percentage of fractured mesas of different sizes at different trench widths. h) Raman shift and in-plane stress of mesa (100 μm) with different trench widths. (a-d) Reproduced with permission.[140] Copyright 2012, John Wiley and Sons. (e-h) Reproduced with permission.[141] Copyright 2018, John Wiley and Sons.

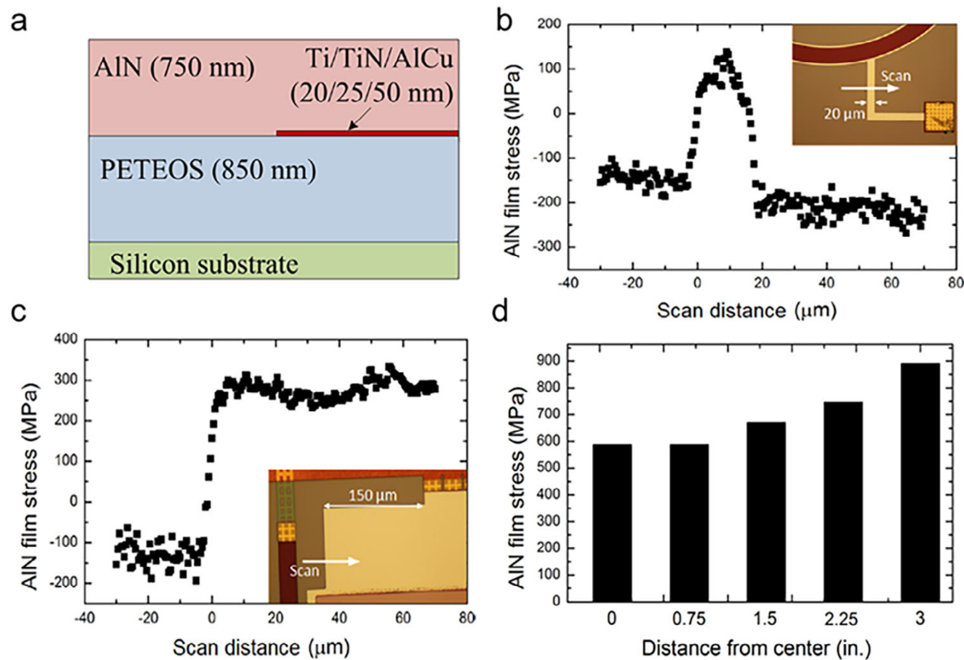

Figure 21. Stress distribution of AlN/metal/PETEOS/Si. a) Schematic of cross-section. Raman-stress relation map of AlN deposited on patterned bottom metal. b) trace and c) rectangular pad. d) Stress distribution on 6 in-AlN/metal/PETEOS/Si sample. Reproduced with permission.[142] Copyright 2016, Institute of Physics Publishing.

significantly contributing to chip protection. Stress analysis during the chip-bonding process is paramount for producing electronic devices. For example, Uchida et al.[143] utilized Raman spectroscopy to evaluate the stress within a silicon-based chip mounted on a copper plate (**Figure** 22a). Their findings, compared with FEM calculations, as depicted in the model in Figure 22b, showed a remarkable alignment between the σ_{11}' values from FEM and Raman measurements. The stress discrepancies at each point were minimal, consistently below 10 MPa, with σ_{11}' closely mirroring σ_{22}', and σ_{33}' being significantly less than σ_{11}' and σ_{22}'. These findings suggest an isotropic biaxial stress on the (001) plane, as shown in Figure 22c. Integrating these analytical techniques provides valuable insights into accurately determining stress in electronic devices, enhancing their precision and reliability. During the die bonding process, the solder type significantly impacts chip-bonding strength. Drawing on prior research, Conti et al.[144] investigated the effect of 3 solder types (AuSn soldering, silver sintering, and copper sintering) on stress distribution during Si chip-bonding to copper substrates. Through 2D Raman scanning of a square Si chip, they observed distinct Raman signal distributions among the solder types. AuSn soldering exhibited an even distribution pattern, exhibiting reverse central symmetry, while copper sintering revealed a symmetry axis on the Si surface, slightly tilted along the diagonal direction of the chip. In contrast, the Si Raman signal's position change in silver sintering remained largely uniform, displaying geometric symmetry.

Silicon-based solar cells also face stress-related challenges during processes such as wafer joining. Hsiao et al.[145] proposed an innovative approach to reduce the thermomechanical stress induced in Si solar cells during the interconnection process (Figure 22d,e), verified through residual stress measurements using Raman spectroscopy. Their approach showed that interconnected Si solar cells underwent reduced tensile stress when using the balanced contact method (Figure 22f,g).

6.4.2. Through Silicon Vias (TSV)

In recent years, TSVs have emerged as critical components in achieving the functionality of 3D high-density ICs. This technology reduces wiring length, interconnection delay, and power consumption, facilitating the creation of high-density stacked ICs and enhancing device performance.[146] However, thermomechanical reliability remains a significant challenge due to stress caused by the mismatch in coefficients of thermal expansion between copper, dielectric materials, and semiconductor substrates. This mismatch can lead to reliability issues, including cracks, delamination, and voids,[147] making the precise characterization of stress in vias critically important.

Kwon et al.[148] explored the stress evolution in Si surrounding a thermally annealed copper-filled TSV structure through micro-Raman spectroscopy. Their findings reveal that the evolution of Si stress post-annealing is closely tied to the initial stress state, as well as the geometry and orientation of the TSV array. **Figure** 23a illustrates the Raman shift and stress in TSVs with a diameter of 10 μm and a pitch of 20 μm, both before and after the annealing process. Before annealing, compressive-stress was observed across the entire Si area with the outer region around the TSV copper structure experiencing higher stress than the

18638899, 2024, 7, Downloaded from https://onlinelibrary.wiley.com/doi/10.1002/lpor.202301300 by Tu Delft, Wiley Online Library on [15/07/2024]. See the Terms and Conditions (https://onlinelibrary.wiley.com/terms-and-conditions) on Wiley Online Library for rules of use; OA articles are governed by the applicable Creative Commons License

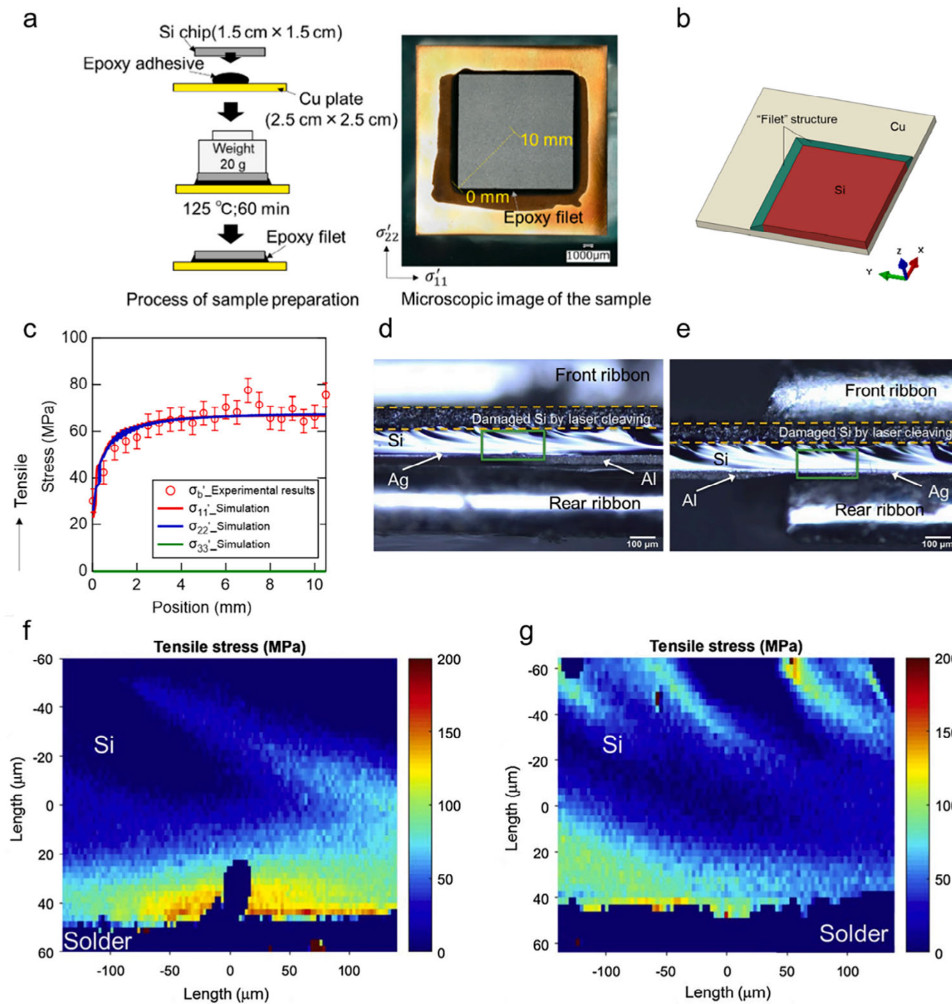

Figure 22. Stress distribution is caused by the die attach process. a) Schematic of the sample preparation process and optical micrograph of the sample. Stress measurements are taken along a yellow dashed line. (b) FEM for Si (001) crystal plane stress simulation. c) Comparison of stress results between Raman measurement and FEM. Cross-sections of solar cells d) without and e) with balanced contact connections. Raman-stress relation mapping of cross-sections of solar cells f) without and g) with balanced contacts. (a-c) Reproduced with permission.[143] Copyright 2021, Elsevier. (d-g) Reproduced with permission.[145] Copyright 2020, Elsevier.

area between TSVs. Post-annealing, a significant increase in compressive-stress near the TSVs and the emergence of tensile stress between diagonal TSVs were noted, showing a four-fold rotational symmetry. Figure 23b, displays the Raman shifts of TSVs with a diameter of 5 µm and a pitch of 10 µm, both before and after thermal annealing. Initially, the stress distribution resembled that of the TSV array with a diameter of 10 µm. However, post-annealing, the Raman shift and stress distribution showed a notable dependence on the excitation wavelength. After annealing, the Si's stress distribution experienced significant changes, as shown in Figure 23c,d. Especially noteworthy is the larger offset observed in the TSV array with wider spacing, attributed to the differing expansion coefficients of Cu and Si during annealing, which led to compressive-stress around the TSV edges. Interestingly, between the 10-micron diameter TSVs, a mix of compressive and tensile stresses was observed, unlike in the 5 µm diameter TSVs. Building on this research, Bayat et al.[149] specifically investigated the effect of annealing temperature on Cu-TSVs. **Figure** 24a illustrates the distribution of Raman frequency shifts of Si around cylindrical copper-filled TSVs before annealing, assessing how annealing at 380 °C for 1 h influenced the reduction of Si's residual stress. The stress in the sample prior to annealing was found to be greater than post-annealing, with a notable decrease in stress change near the Cu/Si interface after annealing. The effect of stress reduction was more pronounced at higher annealing temperatures (Figure 24b).

These findings underscore the significant impact of interconnections in semiconductor packaging on device stress levels. By carefully selecting interconnect technologies, and materials, and incorporating design considerations, it is possible to mitigate stress and improve the performance, reliability, and lifespan of semiconductor devices.

 © 2024 Wiley-VCH GmbH

18638899, 2024, 7, Downloaded from https://onlinelibrary.wiley.com/doi/10.1002/lpor.202301300 by Tu Delft, Wiley Online Library on [15/07/2024]. See the Terms and Conditions (https://onlinelibrary.wiley.com/terms-and-conditions) on Wiley Online Library for rules of use; OA articles are governed by the applicable Creative Commons License

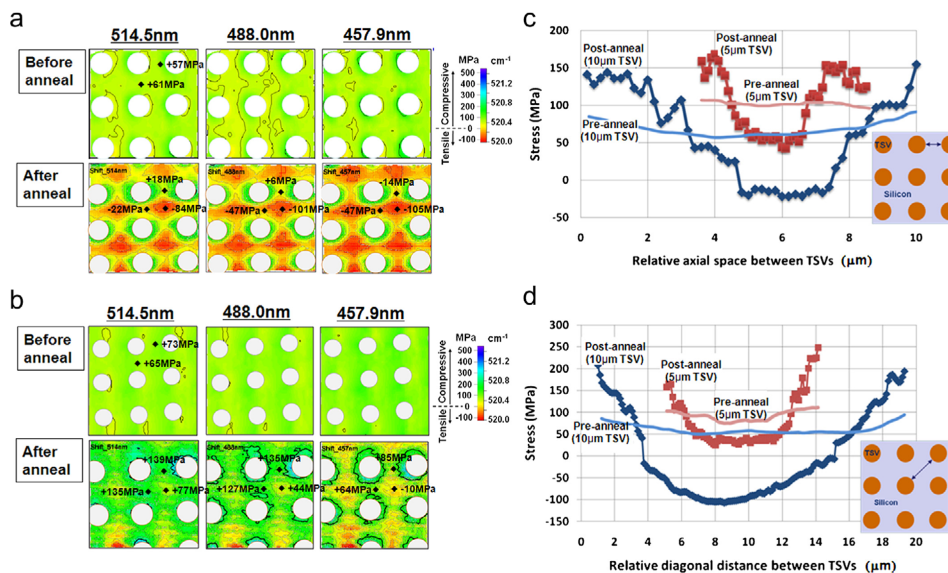

Figure 23. Raman shift and stress evolution diagrams of TSVs arrays before and after annealing. Diameters of TSVs arrays are a) 10 μm and b) 5 μm. Raman laser wavelengths are 514.5, 488.0, and 457.9 nm. Cross-sectional stress variation plots in region between TSVs centers before and after annealing, along c) axial and d) diagonal directions. Reproduced with permission.[148] Copyright 2011, AIP Publishing.

6.5. Flexible Electronics

As electronic device applications continue to evolve and expand, the flexibility of these devices has emerged as a crucial factor for their application in various fields, such as flexible biomedical chips, smart textiles, and flexible displays. However, the enhanced flexibility introduces significant stress challenges during bending and deformation, making stress analysis an essential aspect of their structural design. This analysis is critical in determining the structural integrity and performance of the internal electronic components.

Given the prevalent use of conventional silicon-based devices in the electronics industry, there has been a push toward developing new flexible silicon-based electronic devices. Colinge et al.[150] have made strides in this direction by successfully transferring thin monocrystalline Si films onto flexible and transparent polymer substrates using polymers as adhesives (**Figure 25a**). They employed ultraviolet (UV) micro-Raman spectroscopy to study the residual stress in the transferred substrates. During their analysis, Raman spectra were collected using excitation photons with a wavelength of 514.5 nm, comparing the Raman spectra of bulk and thin-film Si postchemical mechanical polishing and wet etching, respectively (Figure 25b). The observed Raman shifts in the thin Si samples were minor (0.20 and 0.41 cm^{-1} respectively) compared to bulk Si reference values, with calculated stresses of −32 and −65 MPa for the respective samples. Although this research represents a significant advancement in flexible Si thin-film technology, the internal stress distribution within such flexible silicon-based devices remains largely unexplored. Burghartz et al.[151] investigated the uniaxial stress induced by bending ultrathin single-crystal Si chips through Raman spectroscopy. Initial measurements on a flat Si chip (Figure 25c) revealed shifts in the Raman frequency indicating both compressive and tensile stress. Further measurements on the same sample bent over a cylinder with a 10 mm radius showed all measured peaks shifting toward lower frequencies, suggesting dominant tensile stress under blending (Figure 25d). Figure 25e clearly illustrates this uneven stress distribution, decreasing from the center along the bending direction to the edge of the chip and then increasing toward the other edges, underscores the complexity of stress management in ultrathin silicon-based flexible devices.

The emergence of new 2D materials, such as graphene,[152–158] black phosphorus,[159–162] and 2D metal chalcogenides,[162–168] has significantly advanced the development of flexible electronic devices.[169–171] These materials hold great promise for applications in wearable devices, photodetectors, pressure sensors, and beyond. Alongside the advancement of these new devices, extensive research focuses on the impacts of bending stress on actual device performance.[172–175]

The rapid development of novel 2D materials has propelled flexible electronic devices into a new era of progress across various applications. However, to unlock their full potential and secure high performance in these devices, accurate characterization of stress distribution at the microscopic level becomes crucial. Additionally, addressing the issue of fatigue caused by stress during the bending of Si films stands as a critical area for future exploration. By delving into the internal stress dynamics, we can enhance our understanding of device performance within flexible electronics and identify strategies to optimize device functionality.

7. Summary and Outlook

7.1. Summary

This review presents a comprehensive overview from theory to application, including Raman measurement principles, the basic theory of Raman-stress relations, principles for selecting Raman excitation light, and the primary fields of application

© 2024 Wiley-VCH GmbH

18638899, 2024, 7, Downloaded from https://onlinelibrary.wiley.com/doi/10.1002/lpor.202301300 by Tu Delft, Wiley Online Library on [15/07/2024]. See the Terms and Conditions (https://onlinelibrary.wiley.com/terms-and-conditions) on Wiley Online Library for rules of use; OA articles are governed by the applicable Creative Commons License

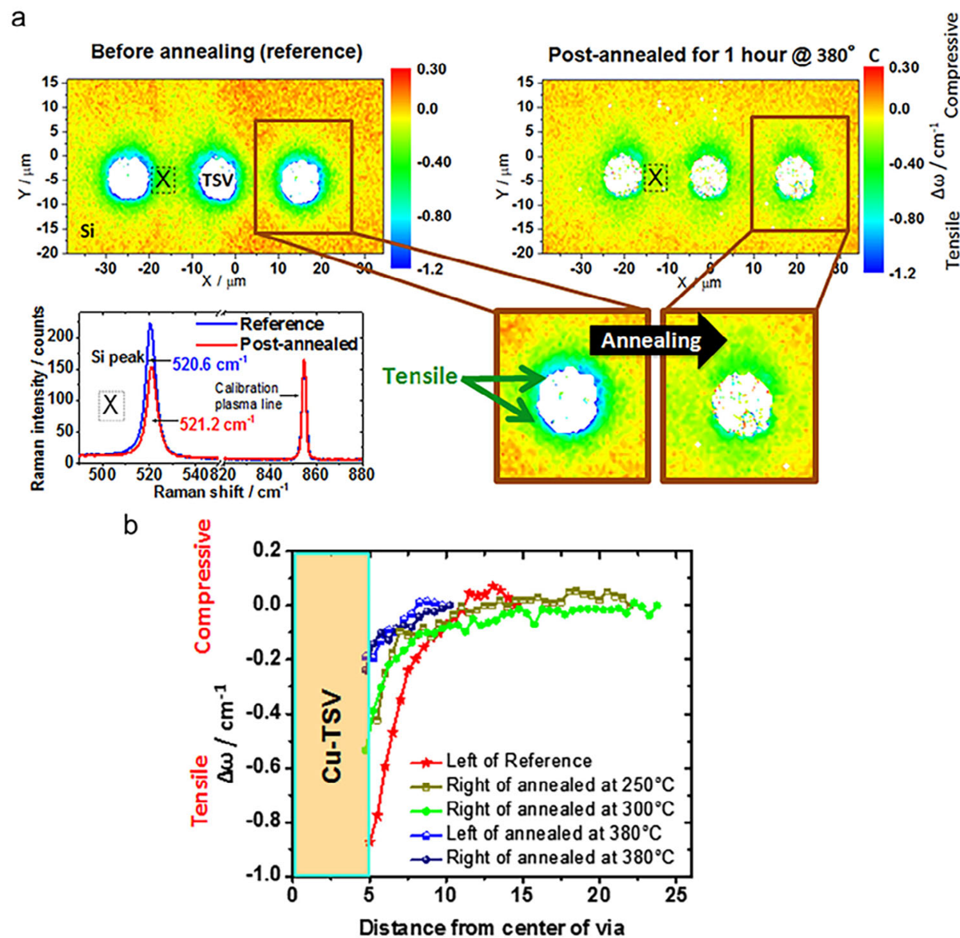

Figure 24. Effect of annealing temperature on Raman shift and stress evolution of TSV. a) Raman frequency shift map of Cu-TSVs population on the Si surface. The left picture is the sample before annealing, and the right picture is the sample after annealing. The spectrum in the lower left corner corresponds to the "X" point. b) Comparison of Raman shifts near TSVs at different annealing temperatures. Reproduced with permission.[149] Copyright 2015, Elsevier.

today. These components are interrelated and collectively influence the accuracy of data in actual testing. Among these, the Raman-stress relations serve as the theoretical foundation for Raman micro-scale mechanics, while the selection of Raman measurement parameters is crucial in actual experimental research. Presently, Raman technology introduces new research directions and testing methodologies for exploring the micro-scale mechanics of electronic devices, aiding in the development of precise stress prediction models and providing insights into the stress behaviors across different crystal planes and within new semiconductor materials. As Raman technology progresses, it has become a key tool for detecting residual stress and exploring the reliability of microelectronic devices. Nonetheless, it is imperative to acknowledge its inherent limitations, notably its constrained depth detection capabilities, typically restricted to surface-level information acquisition. Furthermore, given its reliance on the light scattering mechanism, Raman technology necessitates sample uniformity for optimal performance.

7.2. Outlook

Looking forward, Raman technology holds promise and excitement in the realm of micro-scale mechanics for its natural advantages. For future endeavors in Raman-stress detection, the following recommendations are proposed:

1) Refinement and expansion of Raman-stress relation models: Raman-stress relation models facilitate quick stress detection. However, to address the intricacies of real-world stress conditions and enhance detection accuracy, optimizing and expanding these models is paramount.
2) Detection of stress evolution in the operating environment of microelectronic devices: Considering that internal residual stress in these devices may rise during actual operation, employing in-situ/ex-situ Raman spectroscopy to examine how stress evolution correlates with electrical performance under genuine operating conditions will be a pivotal area of subsequent research. The investigation will enhance the application

 © 2024 Wiley-VCH GmbH

18638899, 2024, 7, Downloaded from https://onlinelibrary.wiley.com/doi/10.1002/lpor.202301300 by Tu Delft, Wiley Online Library on [15/07/2024]. See the Terms and Conditions (https://onlinelibrary.wiley.com/terms-and-conditions) on Wiley Online Library for rules of use; OA articles are governed by the applicable Creative Commons License

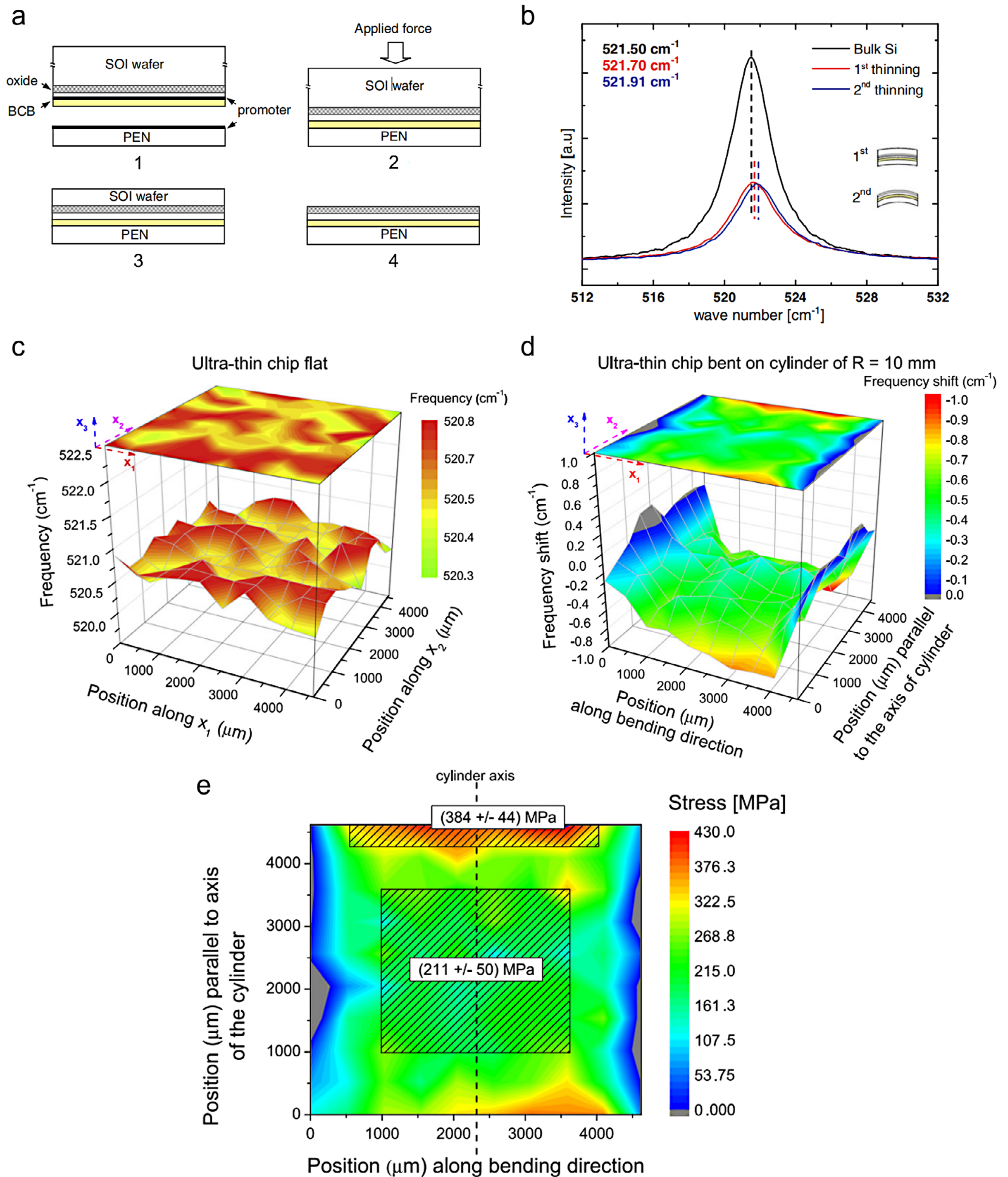

Figure 25. Stress distribution of silicon-based flexible devices. a) Schematic of transfer process of single-crystalline Si to flexible substrates. b) Raman spectroscopy of transferred Si sample based on 514.5 nm Laser. c) Raman spectroscopy of Si chip surface under flat conditions for flexible device. Raman-position d) and stress-position e) mapping of Si surface after bending an ultrathin Si wafer on cylinder. (a,b) Reproduced with permission.[150] Copyright 2010, Springer Nature. (c-e) Reproduced with permission.[151] Copyright 2014, Springer Nature.

© 2024 Wiley-VCH GmbH

18638899, 2024, 7, Downloaded from https://onlinelibrary.wiley.com/doi/10.1002/lpor.202301300 by Tu Delft, Wiley Online Library on [15/07/2024]. See the Terms and Conditions (https://onlinelibrary.wiley.com/terms-and-conditions) on Wiley Online Library for rules of use; OA articles are governed by the applicable Creative Commons License

and development of Raman spectroscopy in microelectronic stress detection.

3) Integration with advanced packaging and structural design: The progression toward highly integrated, densely packed electronic devices necessitates innovations in structural designs and advanced packaging techniques. Understanding the influence of these new designs and processes on residual stress is important. Raman spectroscopy offers an effective evaluation of the feasibility of these innovations with stress considerations.
4) Flexible electronic stress research: Unlike traditional microelectronic devices, the electrical properties of flexible electronics are significantly influenced by the intricate internal stress distribution resulting from various bending and folding states. Investigating the relationship between stress patterns and the real-world performance of flexible electronic devices through Raman spectroscopy is pivotal in promoting flexible electronic technology for practical applications.

Acknowledgements

This work was partially supported by the National Natural Science Foundation of China (52275559), the Shanghai Pujiang Program (2021PJD002), and the Shanghai Science and Technology Development Funds (19DZ2253400).

Conflict of Interest

The authors declare no conflict of interest.

Keywords

microelectronic manufacturing, micro-scale mechanics, Raman-stress relation, residual stress

Received: December 7, 2023
Revised: March 10, 2024
Published online: April 20, 2024

[1] S. Seal, H. Mantooth, *Energies* **2017**, *10*, 341.
[2] R. T. Yadlapalli, A. Kotapati, R. Kandipati, S. R. Balusu, C. S. Koritala, *Int. J. Energ. Res.* **2021**, *45*, 12638.
[3] X. Wang, Z. Yang, B. Wang, W. Chen, G. Zhang, J. Zhang, J. Fan, P. Liu, *J. Mater. Res. Technol.* **2023**, *25*, 6593.
[4] X. Guo, Z. Xue, Y. Zhang, *NPG Asia Mater* **2019**, *11*, 29.
[5] M. Köntges, S. Altmann, T. Heimberg, U. Jahn, K. A. Berger, in Proc. of the 32nd European Photovoltaic Solar Energy Conf. and Exhibition, Munich, Germany **2016**, *6*, 1435.
[6] P. Meszmer, R. D. Rodriguez, E. Sheremet, D. R. T. Zahn, B. Wunderle, *Microelectron Reliab.* **2017**, *79*, 104.
[7] W. Qiu, L. Ma, Q. Li, H. Xing, C. Cheng, G. Huang, *Acta Mech. Sinica-Prc.* **2018**, *34*, 1095.
[8] W. Liu, Q. Li, G. Jin, W. Qiu, *J. Spectrosc.* **2017**, *2017*, 1.
[9] C. Song, L. Du, L. Qi, Y. Li, X. Li, Y. Li, *J. Micromech. Microeng.* **2017**, *27*, 105014.
[10] R. C. Teixeira, I. Doi, M. B. P. Zakia, J. A. Diniz, J. W. Swart, *Mat. Sci. Eng. B* **2004**, *112*, 160.
[11] B. Wunderle, B. Michel, *Microsyst. Technol.* **2009**, *15*, 799.
[12] Q. Li, C.-F. Li, W. Zhang, W. Chen, Z.-Q. Liu, *Microelectron Reliab.* **2019**, *99*, 12.
[13] P. Rostron, S. Gaber, D. Gaber, *laser* **2016**, *6*, 50.
[14] R. S. Das, Y. K. Agrawal, *Vib. Spectrosc.* **2011**, *57*, 163.
[15] A. Orlando, F. Franceschini, C. Muscas, S. Pidkova, M. Bartoli, M. Rovere, A. Tagliaferro, *Chemosensors* **2021**, *9*, 262.
[16] X. X. Han, W. Ji, B. Zhao, Y. Ozaki, *Nanoscale* **2017**, *9*, 4847.
[17] B. Yang, S. Jin, S. Guo, Y. Park, L. Chen, B. Zhao, Y. M. Jung, *ACS Omega* **2019**, *4*, 20101.
[18] V. T. Srikar, S. M. Spearing, *Exp. Mech.* **2003**, *43*, 238.
[19] P. P. Hu, J. Liu, S. X. Zhang, K. Maaz, J. Zeng, H. Guo, P. F. Zhai, J. L. Duan, Y. M. Sun, M. D. Hou, *Nucl. Instrum. Meth. B* **2016**, *372*, 29.
[20] W. Qiu, C.-L. Cheng, R.-R. Liang, C.-W. Zhao, Z.-K. Lei, Y.-C. Zhao, L.-L. Ma, J. Xu, H.-J. Fang, Y.-L. Kang, *Acta. Mech. Sinica-Prc* **2016**, *32*, 805.
[21] L. Sirleto, A. Vergara, M. A. Ferrara, *Adv. Opt. Photonics* **2017**, *9*, 169.
[22] D. W. Shipp, F. Sinjab, I. Notingher, *Adv. Opt. Photonics* **2017**, *9*, 315.
[23] D. Cialla-May, M. Schmitt, J. Popp, *Phys. Sci. Rev* **2019**, *4*, 20170040.
[24] E. Anastassakis, *J. Appl. Phys.* **1997**, *82*, 1582.
[25] F. Cerdeira, C. J. Buchenauer, F. H. Pollak, M. Cardona, *Phys. Rev. B* **1972**, *5*, 580.
[26] M. H. Brodsky, M. Cardona, J. J. Cuomo, *Phys. Rev. B* **1977**, *16*, 3556.
[27] J. Menéndez, M. Cardona, *Phys. Rev. B* **1984**, *29*, 2051.
[28] I. R. Lewis, H. Edwards, *Handbook of Raman Spectroscopy: from the Research Laboratory to the Process Line*, **2001**.
[29] I. De Wolf, H. E. Maes, S. K. Jones, *J. Appl. Phys.* **1996**, *79*, 7148.
[30] C. Kisielowski, J. Kruger, S. Ruvimov, T. Suski, J. W. Ager, 3rd, E. Jones, Z. Liliental-Weber, M. Rubin, E. R. Weber, M. D. Bremser, R. F. Davis, *Phys. Rev. B Condens. Matter.* **1996**, *54*, 17745.
[31] I. Ahmad, M. Holtz, N. N. Faleev, H. Temkin, *J. Appl. Phys.* **2004**, *95*, 1692.
[32] S. Choi, E. Heller, D. Dorsey, R. Vetury, S. Graham, *J. Appl. Phys.* **2013**, *113*, 093510.
[33] H. Wang, N. S. Kim, Y. Song, P. Albertus, S. B. Lee, G. Rubloff, D. Stewart, *Acs Appl. Mater. Inter.* **2023**, *15*, 10752.
[34] H. Wang, Y. Song, V. C. Ferrari, N. S. Kim, S. B. Lee, P. Albertus, G. Rubloff, D. M. Stewart, *Acs Appl. Mater. Inter.* **2023**, *15*, 40409.
[35] B. Han, M. Sun, Y. Chang, S. He, Y. Zhao, C. Qu, W. Qiu, *Mater* **2023**, *16*, 2255.
[36] S. Narayanan, S. R. Kalidindi, L. S. Schadler, *J. Appl. Phys.* **1997**, *82*, 2595.
[37] I. D. Wolf, *Semicond. Sci. Tech.* **1996**, *11*, 139.
[38] C. Schinke, P. C. Peest, J. Schmidt, R. Brendel, K. Bothe, M. R. Vogt, I. Kröger, S. Winter, A. Schirmacher, S. Lim, H. T. Nguyen, D. MacDonald, *AIP Adv.* **2015**, *5*, 067168.
[39] A. D. Rakić, M. L. Majewski, *J. Appl. Phys.* **1996**, *80*, 5909.
[40] D. E. Aspnes, S. M. Kelso, R. A. Logan, R. Bhat, *J. Appl. Phys.* **1986**, *60*, 754.
[41] K. Papatryfonos, T. Angelova, A. Brimont, B. Reid, S. Guldin, P. R. Smith, M. Tang, K. Li, A. J. Seeds, H. Liu, D. R. Selviah, *AIP Adv.* **2021**, *11*, 025327.
[42] S. Adachi, *J. Appl. Phys.* **1989**, *66*, 6030.
[43] T. N. Nunley, N. S. Fernando, N. Samarasingha, J. M. Moya, C. M. Nelson, A. A. Medina, S. Zollner, *J. Vac. Sci. Technol. B* **2016**, *34*, 061205.
[44] L. Y. Beliaev, E. Shkondin, A. V. Lavrinenko, O. Takayama, *J. Vac. Sci. Technol. A* **2021**, *39*, 043408.
[45] T. Kawashima, H. Yoshikawa, S. Adachi, S. Fuke, K. Ohtsuka, *J. Appl. Phys.* **1997**, *82*, 3528.
[46] D. Khmelevskaia, D. I. Markina, V. V. Fedorov, G. A. Ermolaev, A. V. Arsenin, V. S. Volkov, A. S. Goltaev, Y. M. Zadiranov, I. A. Tzibizov,

© 2024 Wiley-VCH GmbH

18638899, 2024, 7, Downloaded from https://onlinelibrary.wiley.com/doi/10.1002/lpor.202301300 by Tu Delft, Wiley Online Library on [15/07/2024]. See the Terms and Conditions (https://onlinelibrary.wiley.com/terms-and-conditions) on Wiley Online Library for rules of use; OA articles are governed by the applicable Creative Commons License

A. P. Pushkarev, A. K. Samusev, A. A. Shcherbakov, P. A. Belov, I. S. Mukhin, S. V. Makarov, *Appl. Phys. Lett.* **2021**, *118*, 201101.
[47] S. Ninomiya, S. Adachi, *J. Appl. Phys.* **1995**, *78*, 1183.
[48] G. A. Ermolaev, Y. V. Stebunov, A. A. Vyshnevyy, D. E. Tatarkin, D. I. Yakubovsky, S. M. Novikov, D. G. Baranov, T. Shegai, A. Y. Nikitin, A. V. Arsenin, V. S. Volkov, *Npj 2D Mater. Appl.* **2020**, *4*, 21.
[49] B. Munkhbat, P. Wrobel, T. J. Antosiewicz, T. O. Shegai, *ACS Photonics* **2022**, *9*, 2398.
[50] S. Ozaki, S. Adachi, *Jpn. J. Appl. Phys.* **1993**, *32*, 5008.
[51] A. B. Djuri˘si´c, E. H. Li, D. Raki´c, M. L. Majewski, *Appl. Phys. A* **2000**, *70*, 29.
[52] S. Ninomiya, S. Adachi, *J. Appl. Phys.* **1995**, *78*, 4681.
[53] S. Adachi, T. Taguchi, *Phys. Rev. B Condens. Matter.* **1991**, *43*, 9569.
[54] S. Adachi, T. Kimura, N. Suzuki, *J. Appl. Phys.* **1993**, *74*, 3435.
[55] K. Sato, S. Adachi, *J. Appl. Phys.* **1993**, *73*, 926.
[56] S. G. Sridhara, R. P. Devaty, W. J. Choyke, *J. Appl. Phys.* **1998**, *84*, 2963.
[57] M. Fan, W. Cen, X. Cai, Y. Liao, J. Xie, Q. Xie, *Appl. Surf. Sci.* **2018**, *427*, 851.
[58] S. G. Sridhara, T. J. Eperjesi, R. P. Devaty, W. J. Choyke, *Mat. Sci. Eng. B* **1999**, 229.
[59] H. Heidarzadeh, A. Rostami, M. Dolatyari, G. Rostami, *J. Photon. Energy* **2014**, *4*, 042098.
[60] X. Zhang, E. Kioupakis, *Phys. Rev. B* **2023**, *107*, 115207.
[61] Z. Zhang, S. Sheng, R. Wang, M. Sun, *Anal. Chem.* **2016**, *88*, 9328.
[62] E. V. Efremov, F. Ariese, C. Gooijer, *Anal. Chim. Acta* **2008**, *606*, 119.
[63] D. Wei, S. Chen, Q. Liu, *Appl. Spectrosc. Rev.* **2015**, *50*, 387.
[64] G. Ferraris, J. Dubessy, M. C. Caumon, F. Rull, *EMU Notes Mineral.* **2012**, *12*, 1.
[65] E. Anastassakis, A. Pinczuk, E. Burstein, F. H. Pollak, M. Cardona, *Solid State Commun.* **1970**, *8*, 133.
[66] I. De Wolf, J. Vanhellemont, A. Romano-Rodríguez, H. Norström, H. E. Maes, *J. Appl. Phys.* **1992**, *71*, 898.
[67] I. De Wolf, M. Ignat, G. Pozza, L. Maniguet, H. E. Maes, *J. Appl. Phys.* **1999**, *85*, 6477.
[68] C. Jian, I. De Wolf, *IEEE T Compon. Pack T* **2005**, *28*, 484.
[69] Y. Kang, Y. Qiu, Z. Lei, M. Hu, *Opt. Laser Eng.* **2005**, *43*, 847.
[70] I. De Wolf, *J. Appl. Phys.* **2015**, *118*, 053101.
[71] L. Ma, X. Fan, W. Qiu, *Opt. Lett.* **2019**, *44*, 4682.
[72] J. Millán, in *Data Mining: Foundations and Intelligent Paradigms*, Springer, Espoo, Finland **2012**, *10*, 57.
[73] S. Fujita, *Jpn. J. Appl. Phys.* **2015**, *54*, 030101.
[74] Y. F. Chen, X. Z. Liu, X. W. Deng, Y. R. Li, *Thin Solid Films* **2009**, *517*, 2882.
[75] M. Yoshikawa, Y. Fujita, M. Murakami, *Appl. Spectrosc.* **2019**, *73*, 1193.
[76] Q. Kang, X. Fang, C. Wu, H. Sun, Z. Fang, B. Tian, L. Zhao, S. Wang, N. Zhu, P. Verma, M. Ryutaro, Z. Jiang, *Ceram. Int.* **2022**, *48*, 27076.
[77] C. J. Lee, G. Pezzotti, Y. Okui, S. Nishino, *Appl. Surf. Sci.* **2004**, *228*, 10.
[78] K. R. Bagnall, E. A. Moore, S. C. Badescu, L. Zhang, E. N. Wang, *Rev. Sci. Instrum.* **2017**, *88*, 113111.
[79] L. Zhu, X. Tang, J. Wang, Y. Hou, *AIP Adv.* **2019**, *9*, 015024.
[80] S. Webster, D. N. Batchelder, D. A. Smith, *Appl. Phys. Lett.* **1998**, *72*, 1478.
[81] X. Wu, J. Yu, T. Ren, L. Liu, *Microelectron J.* **2007**, *38*, 87.
[82] G. Lucazeau, L. Abello, *J. Mater. Res.* **1996**, *12*, 2262.
[83] E. Bonera, M. Fanciulli, D. N. Batchelder, *Appl. Phys. Lett.* **2002**, *81*, 3377.
[84] E. Bonera, M. Fanciulli, D. N. Batchelder, *J. Appl. Phys.* **2003**, *94*, 2729.
[85] Y. Gogotsi, C. Baek, F. Kirscht, *Semicond. Sci. Tech.* **1999**, *14*, 936.
[86] M. A. Druy, R. A. Crocombe, D. P. Bannon, M. De Biasio, L. Neumaier, N. Vollert, E. Geier, M. Roesner, C. Hirschl, M. Kraft, in *Next-Generation Spectroscopic Technologies VIII*, SPIE, **2015**.
[87] W. Qiu, L.-l. Ma, H.-D. Xing, C.-L. Cheng, G. Huang, *AIP Adv.* **2017**, *7*, 075002.
[88] V. Pogue, S. N. Melkote, S. Danyluk, *Mat. Sci. Semicon. Proc.* **2018**, *75*, 173.
[89] L. Ma, H. Xing, Q. Li, J. Wang, W. Qiu, *Jpn. J. Appl. Phys.* **2018**, *57*, 080307.
[90] R. Adappa, K. Suryanarayana, H. S. Hatwar, M. R. Rao, in 2019 2nd International Conf. on Intelligent Computing, Instrumentation and Control Technologies (ICICICT), IEEE Xplore, Kannur, India **2019**, 1197.
[91] E. del Corro, J. G. Izquierdo, J. González, M. Taravillo, V. G. Baonza, *J. Raman Spectrosc.* **2013**, *44*, 758.
[92] N. Sugiyama, M. Yamada, Y. Urakami, M. Kobayashi, T. Masuda, K. Nishikawa, F. Hirose, S. Onda, *MRS OPL* **2014**, *1693*, 14.
[93] D. P. Mohanty, H. Wang, M. Okuniewski, V. Tomar, *J. Nucl. Mater.* **2017**, *497*, 128.
[94] H. Shi, Q. Song, Y. Hou, S. Yue, Y. Li, Z. Zhang, M. Li, K. Zhang, Z. Zhang, *Ceram. Int.* **2022**, *48*, 24276.
[95] M. Iwinska, M. Amilusik, M. Fijalkowski, T. Sochacki, B. Lucznik, E. Grzanka, E. Litwin-Staszewska, J. L. Weyher, A. Nowakowska-Siwinska, G. Muziol, C. Skierbiszewski, I. Grzegory, E. Guiot, R. Caulmilone, M. Bockowski, *J. Cryst. Growth* **2016**, *456*, 73.
[96] E. A. Jones, F. F. Wang, D. Costinett, *Ieee J. Em. Sel. Top P* **2016**, *4*, 707.
[97] N. Islam, M. F. P. Mohamed, M. F. A. J. Khan, S. Falina, H. Kawarada, M. Syamsul, *Crystals* **2022**, *12*, 1581.
[98] J. Kim, K. Baik, C. Park, S. Cho, S. J. Pearton, F. Ren, *Phys. Status Solidi A* **2006**, *203*, 2393.
[99] M. Lee, S. Park, *RSC Adv.* **2018**, *8*, 35571.
[100] S. M. Langan, D. Ravindra, A. B. Mann, *Precis. Eng.* **2019**, *56*, 1.
[101] A. Nagaraj, S. Min, *CIRP Ann.* **2022**, *71*, 101.
[102] M. Chu, A. D. Koehler, A. Gupta, T. Nishida, S. E. Thompson, *J. Appl. Phys.* **2010**, *108*, 104502.
[103] C. Kisielowski, J. Kru¨ger, S. Ruvimov, T. Suski, J. W. A. III, E. Jones, Z. Liliental-Weber, M. Rubin, E. R. Weber, *Phys. Rev. B* **1996**, *54*, 17745.
[104] S. C. Binari, P. B. Klein, T. E. Kazior, *P IEEE* **2002**, *90*, 1048.
[105] F. A. Ponce, *MRS Bull.* **2013**, *22*, 51.
[106] J. Mickevičius, M. S. Shur, R. S. Q. Fareed, J. P. Zhang, R. Gaska, G. Tamulaitis, *Appl. Phys. Lett.* **2005**, *87*, 2419198.
[107] M. Shur, R. Gaska, A. Dobrinsky, M. Shatalov, *ECS Trans.* **2014**, *61*, 53.
[108] J. López, E. Solorio, H. A. Borbón-Nuñez, F. F. Castillón, R. Machorro, N. Nedev, M. H. Farías, H. Tiznado, *J. Alloy Compd.* **2017**, *691*, 308.
[109] R. Zhu, H. He, Z. Lin, S. Jiang, J. Zhang, *Mater. Today Commun.* **2020**, *24*, 101143.
[110] K. Ito, N. Kikuchi, T. Seki, K. Takanashi, *J. Magn. Magn. Mater.* **2022**, *563*, 169908.
[111] R. Huang, S. L. Benjamin, C. Gurnani, Y. Wang, A. L. Hector, W. Levason, G. Reid, C. H. De Groot, *Sci. Rep.* **2016**, *6*, 27593.
[112] M. Mohammadi Ghaleni, E. Tavakoli, M. Bavarian, S. Nejati, *AIChE J.* **2020**, *66*, e17019.
[113] O. Delorme, L. Cerutti, E. Luna, A. Trampert, E. Tournié, J. B. Rodriguez, *J. Appl. Phys.* **2019**, *126*, 155304.
[114] F. Krizek, Z. Kašpar, A. Vetushka, D. Kriegner, E. M. Fiordaliso, J. Michalicka, O. Man, J. Zubáč, M. Brajer, V. A. Hills, K. W. Edmonds, P. Wadley, R. P. Campion, K. Olejník, T. Jungwirth, V. Novák, *Phys. Rev. Mater.* **2020**, *4*, 014409.
[115] C. Bradac, W. Gao, J. Forneris, M. E. Trusheim, I. Aharonovich, *Nat. Commun.* **2019**, *10*, 5625.

© 2024 Wiley-VCH GmbH

18638899, 2024, 7, Downloaded from https://onlinelibrary.wiley.com/doi/10.1002/lpor.202301300 by Tu Delft, Wiley Online Library on [15/07/2024]. See the Terms and Conditions (https://onlinelibrary.wiley.com/terms-and-conditions) on Wiley Online Library for rules of use; OA articles are governed by the applicable Creative Commons License

[116] N. Donato, N. Rouger, J. Pernot, G. Longobardi, F. Udrea, *J. Phys. D Appl. Phys.* **2019**, *53*, 093001.
[117] M. Mermoux, B. Marcus, A. Crisci, A. Tajani, E. Gheeraert, E. Bustarret, *J. Appl. Phys.* **2005**, *97*, 043530.
[118] R. Ahmed, M. Nazari, B. L. Hancock, J. Simpson, C. Engdahl, E. L. Piner, M. W. Holtz, *Appl. Phys. Lett.* **2018**, *112*, 181907.
[119] F. Isa, J. P. Best, A. Marzegalli, M. Albani, C. Comte, J. J. Kruzic, A. Bendavid, *APL Mater.* **2021**, *9*, 061109.
[120] X. She, A. Q. Huang, Ó. Lucía, B. Ozpineci, *IEEE T Ind. Electron* **2017**, *64*, 8193.
[121] W. L. Zhu, J. L. Zhu, S. Nishino, G. Pezzotti, *Appl. Surf. Sci.* **2006**, *252*, 2346.
[122] T. S. Perova, J. Wasyluk, S. A. Kukushkin, A. V. Osipov, N. A. Feoktistov, S. A. Grudinkin, *Nanoscale Res. Lett.* **2010**, *5*, 1507.
[123] F. L. Via, M. Mauceri, V. Scuderi, C. Calabretta, M. Zimbone, R. Anzalone, *Mater. Sci. Forum* **2020**, *1004*, 120.
[124] T. Dn, W. L., T. Cc, F. Zc, *J. Mater. Sci. Eng.* **2017**, *6*, 1000324.
[125] V. Scuderi, M. Zielinski, F. L. Via, *Mater* **2023**, *16*, 3824.
[126] N. Kaminski, O. Hilt, *Iet. Circ. Device Syst.* **2014**, *8*, 227.
[127] A. S. Augustine Fletcher, D. Nirmal, J. Ajayan, L. Arivazhagan, *Aeu-Int. J. Electron C* **2019**, *99*, 325.
[128] J. Xu, L. Gu, Z. Ye, S. Kargarrazi, J. M. Rivas-Davila, *IEEE T Power Electr.* **2020**, *35*, 6340.
[129] A. C. Liu, Y. Y. Lai, H. C. Chen, A. P. Chiu, H. C. Kuo, *Micromachines* **2023**, *14*, 764.
[130] B. L. Hancock, M. Nazari, J. Anderson, E. Piner, F. Faili, S. Oh, D. Twitchen, S. Graham, M. Holtz, *Appl. Phys. Lett.* **2016**, *108*, 211901.
[131] A. S. Grashchenko, S. A. Kukushkin, A. V. Osipov, A. V. Redkov, *J. Phys. Chem. Solids* **2017**, *102*, 151.
[132] Y. Hou, M. Zhang, G. Han, C. Si, Y. Zhao, J. Ning, *J. Semicond.* **2016**, *37*, 101001.
[133] O. Legrani, T. Aubert, O. Elmazria, A. Bartasyte, P. Nicolay, A. Talbi, P. Boulet, J. Ghanbaja, D. Mangin, *IEEE T Ultrason. Ferr.* **2016**, *63*, 898.
[134] F. Dong, R. Li, G. Wu, K. Liang, G. Li, Y. Nie, Z. Gan, Q. Cao, X. Wang, Q. Zhao, S. Liu, *Appl. Phys. Lett.* **2020**, *116*, 54101.
[135] H. Yoshida, S. Kimura, *J. Cryst. Growth* **2020**, *537*, 125605.
[136] Y. Zhu, R. Lin, W. Zheng, J. Ran, F. Huang, *Sci. Bull.* **2020**, *65*, 827.
[137] D. Solonenko, C. Schmidt, C. Stoeckel, K. Hiller, D. R. T. Zahn, *Phys. Status Solidi. B* **2019**, *257*, 1900400.
[138] J. Yin, D. Chen, H. Yang, Y. Liu, D. N. Talwar, T. He, I. T. Ferguson, K. He, L. Wan, Z. C. Feng, *J. Alloy. Compd.* **2021**, *857*, 157487.
[139] C. Wang, X.-D. Gao, D.-D. Li, J.-J. Chen, J.-F. Chen, X.-M. Dong, X. Wang, J. Huang, X.-H. Zeng, K. Xu, *Chinese Phys. B* **2023**, *32*, 026802.
[140] T. Hossain, J. Wang, E. Frayssinet, S. Chenot, M. Leroux, B. Damilano, F. Demangeot, L. Durand, A. Ponchet, M. J. Rashid, F. Semond, Y. Cordier, *Phys. Status Solidi C* **2012**, *10*, 425.
[141] T. Hossain, M. J. Rashid, E. Frayssinet, N. Baron, B. Damilano, F. Semond, J. Wang, L. Durand, A. Ponchet, F. Demangeot, Y. Cordier, *Phys. Status Solidi. B* **2018**, *255*, 1700399.
[142] S. Choi, B. A. Griffin, *J. Micromech. Microeng.* **2016**, *26*, 025009.
[143] T. Uchida, T. Masuyama, R. Sugie, S. Watanabe, *Microelectron Reliab.* **2021**, *121*, 114132.
[144] J. Pascucci, F. Conti, S. K. Bhogaraju, R. Signorini, E. Liu, D. Pedron, G. Elger, P. Cheben, J. Čtyroký, I. Molina-Fernández, in *Integrated Optics: Design, Devices, Systems and Applications VI*, International Society for Optics and Photonics (SPIE), Bellingham, Washington, USA **2021**, *11775*, 132.
[145] P.-C. Hsiao, X. Shen, Z. Wang, N. Song, Y. Li, Z. Ouyang, C. Zhu, J. Lv, C. Shen, C. Chen, G. Chen, A. Lennon, *Sol. Energ. Mat. Sol. C* **2020**, *215*, 110667.
[146] H.-A. S. Shin, B.-J. Kim, J.-H. Kim, S.-H. Hwang, A. S. Budiman, H.-Y. Son, K.-Y. Byun, N. Tamura, M. Kunz, D.-I. Kim, Y.-C. Joo, *J. Electron. Mater.* **2012**, *41*, 712.
[147] A. Heryanto, W. N. Putra, A. Trigg, S. Gao, W. S. Kwon, F. X. Che, X. F. Ang, J. Wei, R. I. Made, C. L. Gan, K. L. Pey, *J. Electron. Mater.* **2012**, *41*, 2533.
[148] W. S. Kwon, D. T. Alastair, K. H. Teo, S. Gao, T. Ueda, T. Ishigaki, K. T. Kang, W. S. Yoo, *Appl. Phys. Lett.* **2011**, *98*, 232106.
[149] P. Bayat, D. Vogel, R. D. Rodriguez, E. Sheremet, D. R. T. Zahn, S. Rzepka, B. Michel, *Microelectron. Eng.* **2015**, *137*, 101.
[150] K. Y. Byun, I. Ferain, S. Song, S. Holl, C. Colinge, *J. Electron. Mater.* **2010**, *39*, 2233.
[151] N. Wacker, H. Richter, T. Hoang, P. Gazdzicki, M. Schulze, E. A. Angelopoulos, M.-U. Hassan, J. N. Burghartz, *Semicond. Sci. Tech.* **2014**, *29*, 095007.
[152] M. Huang, H. Yan, C. Chen, D. Song, T. F. Heinz, J. Hone, *P Natl. Acad. Sci.* **2009**, *106*, 7304.
[153] Y.-H. Lee, Y.-J. Kim, *Appl. Phys. Lett.* **2012**, 101.
[154] W. J. Liu, X. W. Sun, X. A. Tran, Z. Fang, Z. R. Wang, F. Wang, L. Wu, J. F. Zhang, J. Wei, H. L. Zhu, H. Y. Yu, *IEEE T Device Mat. Re.* **2012**, *12*, 478.
[155] L. Peng, Z. Xu, Z. Liu, Y. Guo, P. Li, C. Gao, *Adv. Mater.* **2017**, *29*, 1700589.
[156] Y. Wang, Y. Wang, C. Xu, X. Zhang, L. Mei, M. Wang, Y. Xia, P. Zhao, H. Wang, *Carbon* **2018**, *134*, 37.
[157] H. P. Zhou, X. Ye, W. Huang, M. Q. Wu, L. N. Mao, B. Yu, S. Xu, I. Levchenko, K. Bazaka, *Acs Appl. Mater. Inter.* **2019**, *11*, 15122.
[158] H. Du, Y. Kang, C. Xu, T. Xue, W. Qiu, H. Xie, *Opt. Laser Eng.* **2022**, *149*, 106825.
[159] A. Castellanos-Gomez, L. Vicarelli, E. Prada, J. O. Island, K. L. Narasimha-Acharya, S. I. Blanter, D. J. Groenendijk, M. Buscema, G. A. Steele, J. V. Alvarez, H. W. Zandbergen, J. J. Palacios, H. S. J. van der Zant, *2D Mater.* **2014**, *1*, 025001.
[160] L. Li, Y. Yu, G. J. Ye, Q. Ge, X. Ou, H. Wu, D. Feng, X. H. Chen, Y. Zhang, *Nat. Nanotechnol.* **2014**, *9*, 372.
[161] H. Liu, Y. Du, Y. Deng, P. D. Ye, *Chem. Soc. Rev.* **2015**, *44*, 2732.
[162] B. Karki, B. Freelon, M. Rajapakse, R. Musa, S. M. S. Riyadh, B. Morris, U. Abu, M. Yu, G. Sumanasekera, J. B. Jasinski, *Nanotechnology* **2020**, *31*, 425707.
[163] B. Radisavljevic, A. Radenovic, J. Brivio, V. Giacometti, A. Kis, *Nat. Nanotechnol.* **2011**, *6*, 147.
[164] A. L. Elías, N. Perea-López, A. Castro-Beltrán, A. Berkdemir, R. Lv, S. Feng, A. D. Long, T. Hayashi, Y. A. Kim, M. Endo, H. R. Gutiérrez, N. R. Pradhan, L. Balicas, T. E. Mallouk, F. López-Urías, H. Terrones, M. Terrones, **2013**, *ACS Nano 7*, 5235.
[165] D. Kong, H. Wang, J. J. Cha, M. Pasta, K. J. Koski, J. Yao, Y. Cui, *Nano Lett.* **2013**, *13*, 1341.
[166] H. Li, J. Wu, Z. Yin, H. Zhang, *Accounts Chem. Res.* **2014**, *47*, 1067.
[167] D. Lembke, S. Bertolazzi, A. Kis, *Accounts Chem. Res.* **2015**, *48*, 100.
[168] A. S. Aji, P. Solís-Fernández, H. G. Ji, K. Fukuda, H. Ago, *Adv. Funct. Mater.* **2017**, *27*, 1703448.
[169] L. Gao, *Small* **2017**, *13*, 1603994.
[170] M. Zou, Y. Ma, X. Yuan, Y. Hu, J. Liu, Z. Jin, *J. Semicond.* **2018**, *39*, 011010.
[171] S. Aftab, S. Hussain, A. A. Al-Kahtani, *Adv. Mater.* **2023**, *35*, 2301280.
[172] J.-H. Seo, J. Li, J. Lee, S. Gong, J. Lin, H. Jiang, Z. Ma, *IEEE Photonics J.* **2015**, *7*, 1.
[173] H. H. Choi, H. T. Yi, J. Tsurumi, J. J. Kim, A. L. Briseno, S. Watanabe, J. Takeya, K. Cho, V. Podzorov, *Adv. Sci.* **2019**, *7*, 1901824.
[174] S. An, S. Wu, C. S. Tan, G.-E. Chang, X. Gong, M. Kim, *J. Mater. Chem. C* **2020**, *8*, 13557.
[175] S. An, Y.-C. Tai, K.-C. Lee, S.-H. Shin, H. H. Cheng, G.-E. Chang, M. Kim, *Nanotechnology* **2021**, *32*, 355704.

© 2024 Wiley-VCH GmbH

18638899, 2024, 7, Downloaded from https://onlinelibrary.wiley.com/doi/10.1002/lpor.202301300 by Tu Delft, Wiley Online Library on [15/07/2024]. See the Terms and Conditions (https://onlinelibrary.wiley.com/terms-and-conditions) on Wiley Online Library for rules of use; OA articles are governed by the applicable Creative Commons License

Zhoudong Yang, Ph.D. student, is presently engaged in his study at the Academy for Engineering and Technology, Fudan University, Shanghai. His research focuses on the material interface mechanics and structural reliability in semiconductor devices.

Xinyue Wang, Ph.D. student, is currently engaged in her study at the Academy for Engineering and Technology, Fudan University, Shanghai. Her research interests are in advanced packaging interconnect materials and reliability for wide bandgap semiconductors.

Wei Chen, a Ph.D. student, is currently engaged in his studies at the Academy for Engineering & Technology, Fudan University, Shanghai, China. His main research interests include advanced packaging technology for SiC power electronics, and reliability assessment and failure mechanism analysis of electronic devices.

Hongyu Tang received her Ph.D. in microelectronics from the Department of Microelectronics, Delft University of Technology, Delft, the Netherlands, in 2020. She worked as a postdoctoral fellow at École Polytechnique Fédérale de Lausanne (EPFL), Lausanne, Switzerland, from 2020 to 2022. Now she is an assistant professor at the Academy for Engineering & Technology, Fudan University, Shanghai, China. Her research interests include microelectronics, optoelectronics, and nanodevices for applications.

© 2024 Wiley-VCH GmbH

18638899, 2024, 7, Downloaded from https://onlinelibrary.wiley.com/doi/10.1002/lpor.202301300 by Tu Delft, Wiley Online Library on [15/07/2024]. See the Terms and Conditions (https://onlinelibrary.wiley.com/terms-and-conditions) on Wiley Online Library for rules of use; OA articles are governed by the applicable Creative Commons License

Rongjun Zhang received his B.S. degree in Physics from Center China Normal University, in 1994, and his Ph.D. degree in Solid State Physics from Fudan University, in 1999. He is a full Professor in the School of Information Science and Technology, Academy for Engineering and Technology, Fudan University. During 2003–2004, he worked at Kiel University, Kiel, Germany, as a visiting professor. From 2004–2006, he worked at the Max-Planck Institute for Microstructure Physics, Halle, Germany, as an Alexander von Humboldt Research Fellow. His research interest mainly focuses on the optical properties of solids, intelligent lighting, and health.

Xuejun Fan received a B.S. and M.S. degrees in Applied Mechanics from Tianjin University, Tianjin, China, in 1984 and 1986, respectively, and a Ph.D. degree in Solid Mechanics from Tsinghua University, Beijing, China, in 1989. He is a Professor in the Department of Mechanical Engineering at Lamar University, Beaumont, Texas. His current research interests lie in the areas of design, modeling, material characterization, and reliability in heterogeneous electronic systems.

Guoqi Zhang received a Ph.D. degree in aerospace engineering from Delft University of Technology, Delft, The Netherlands, in 1993. Since 2013, he has been a Chair Professor with the Department of Microelectronics, Delft University of Technology, The Netherlands. His research interests include heterogeneous micro/nanoelectronics packaging, system integration, and reliability.

Jiajie Fan is a Youth Professor at the Academy for Engineering & Technology and Shanghai Research Center for Silicon Carbide Power Devices Engineering & Technology, Fudan University, Shanghai 200 433, China. He is also working as a guest research scientist at the Delft University of Technology, The Netherlands. His main research interests include LED packaging and system integration, Prognostics and health management, and Wide bandgap power electronics packaging.

© 2024 Wiley-VCH GmbH

18638899, 2024, 7, Downloaded from https://onlinelibrary.wiley.com/doi/10.1002/lpor.202301300 by Tu Delft, Wiley Online Library on [15/07/2024]. See the Terms and Conditions (https://onlinelibrary.wiley.com/terms-and-conditions) on Wiley Online Library for rules of use; OA articles are governed by the applicable Creative Commons License